Master Thesis

Master's Degree In Energy Engineering

Analysis of Hybrid LCC-VSC HVDC Transmission Systems

Author: Jie Song

Supervisors: Marc Cheah Mañé
Oriol Gomis Bellmunt

June 2018

Escola Tècnica Superior
d'Enginyeria Industrial de Barcelona

Abstract

High voltage direct current (HVDC) is a highly efficient alternative for transmitting bulk electricity over a long distance. Also, with its high controllability and flexibility, HVDC has been considered as the key enabler in the future energy system based on renewables.

The Line Commutated Converter (LCC) and Voltage Source Converter (VSC) are two technologies that are being widely used in high voltage direct current (HVDC) power transmission. The hybrid connection of LCC and VSC provides a promising solution of HVDC that combines the advantages of both converter technologies.

This thesis presents the modelling, control system design and simulation of hybrid LCC-VSC HVDC system. Different configurations of point-to-point hybrid HVDC connection have been compared. Furthermore, small-signal models have been developed for hybrid HVDC transmission system. The small-signal models are validated through the comparison of non-linear model simulation results. Based on the small-signal model, the system stability and interactions have been analyzed. All simulation results presented in this thesis are shown using MATLAB Simulink R2017a.

Index

List of Figures

List of Tables

1. Introduction

1.1. Research Background

High Voltage Direct Current (HVDC) is widely considered as an efficient and economical option for long distances transmission of electric power compared to AC transmission [1][2]. Conventional HVDC transmission is based on line commutated converter (LCC). Although this mature technology has large transmission capacity, it still has some disadvantages such as the risk of commutation failure, lack of black start capability and large reactive power consumption [3]. Voltage source converter (VSC) based HVDC is a more recent technology that provides higher operational flexibility including independent control of active and reactive power as well as black start capability. However, VSCs have higher switching losses and construction costs compared to LCCs.

On the current stage, Hybrid HVDC with LCCs and VSCs presented a promising alternative solution that combines the advantages of both converter topologies: reduction of power losses and cost and higher control flexibility [4][5][6]. Besides, the conception of hybrid LCC-VSC HVDC can be applied to upgrade the existing LCC-HVDC connection by replacing one of the terminals with VSC. Also, the LCC-HVDC and VSC-HVDC system can be interconnected to build a new hybrid network [7]. However, since the control strategy and operation method of the LCC and VSC is totally different. It is necessary to conduct a study on the operation and control of the hybrid LCC-VSC HVDC transmission system [8].

This thesis, at first, analyzed the basics of HVDC system VSC-HVDC and LCC HVDC respectively. Analytical models were established to verify the designed controllers and to demonstrate the features of these two converter topologies. On the basis of the study above, a point-to-point hybrid HVDC transmission system model has been built by interconnecting the VSC and the LCC to investigate different operation principles and control strategies of hybrid HVDC system. Furthermore, a small-signal model has been developed to analyze the system stability and interactions.

1.2. Research Questions

Through the reviewing of related publications, currently, latest research can be found focusing on various aspects of the hybrid LCC-VSC HVDC. It is believed that a comprehensive study of the hybrid HVDC system, including the modelling, control system design and small-signal

model analysis, will promote the research work on hybrid HVDC and will lay a solid background for the future study on super grid and global energy interconnection.

1.3. Thesis Goals

Based on the research background, the targets of the thesis are set as follows:

- To understand the theoretical background of LCC based HVDC and VSC-HVDC.
- To model and analyze different configurations of point-to-point hybrid LCC-VSC HVDC transmission system.
- To build the small-signal model for different HVDC topologies and configurations. Also, based on the verified small-signal model, the analysis of dynamics and stability will be conducted.
- To design the control system and appropriate operation strategy for the hybrid HVDC system.

1.4. Thesis Outline

The thesis is organized in the following structure:

- Chapter 2 presents the basics of LCC-HVDC. An analytical model has been built in this part. Also, the control scheme has been studied.
- Chapter 3 investigates the basics of VSC-HVDC, including the modelling of a point-to-point VSC-HVDC transmission system and the design of the converter control scheme.
- Chapter 4 investigates the basics of hybrid LCC-VSC HVDC, including the modelling of a point-to-point transmission system. Also, this chapter proposed the start-up strategy of the hybrid HVDC system.
- Chapter 5 includes the construction of the small-signal modelling of hybrid LCC-VSC HVDC. Also, a sensitivity analysis have been conducted based on the linear model of hybrid HVDC system in this chapter.
- Chapter 6 presents conclusion of the thesis. Different configurations of hybrid LCC-VSC HVDC have been compared. Also, the task accomplished in this thesis and the possible future extension are summarized here.

2. LCC-HVDC System

2.1. Introduction to LCC-HVDC

The LCC-based High Voltage Direct-Current Transmission (HVDC) has been used in more than 150 point-to-point installations worldwide [9]. The LCC HVDC has been proven to be technologically mature.

A typical configuration for a LCC HVDC system is based on a 12-pulse connection with monopole operation mode as shown in Figure 2.1. Terminal 1 stands for the rectifier station which converts power from the AC grid to DC network, while terminal 2 is the inverter station connecting the receiving end AC grid.

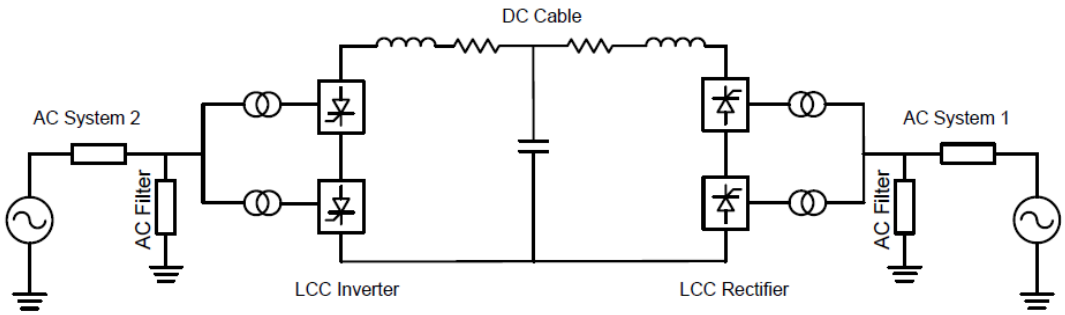

Figure 2.1 Schematic diagram of a typical LCC HVDC

As shown in Figure 2.1, the major components in a typical three-phase LCC HVDC system include :

- *Converters.* Usually include of two six-pulse thyristors bridges.
- *Transformers.* Can be either two units of two-winding tranformaers or one three-winding transformer for each terminal.
- *DC side smoothing reactors.* Typical inductance for large HVDC systems is 0.1–0.5 H, which is d considering DC fault responses, commutation failure, dynamic stability and power quality.

2.2. LCC-HVDC Modelling

2.2.1. LCC Rectifier Modelling

LCC is based on thyristors, the term line-commutated indicates that its commutation from one

switch to another relies on the line voltage of the AC system to which the converter is connected in [9]. A typical three-phase line-commutated converter topology is shown in Figure 2.2 [2].

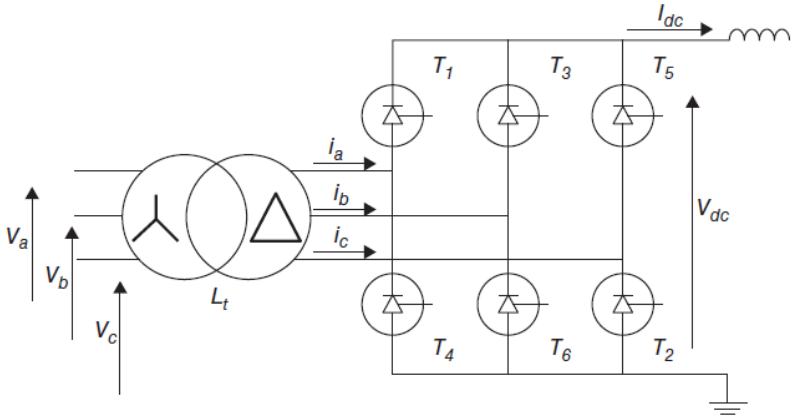

Figure 2.2 Six-pulse thyristor converter with a transformer

And Figure 2.3 shows the AC phase current and DC voltage waveforms of an LCC terminal.

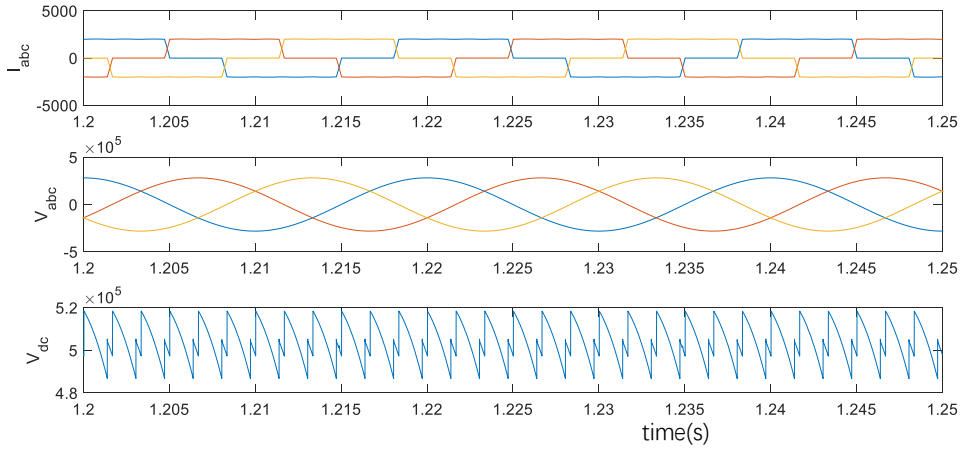

Figure 2.3 Current and voltage waveforms of a six-pulse thyristor converter

If we neglect the commutation overlap, the average value of the DC voltage can be calculated as [10]:

$$\begin{aligned} V_{dc0} &= 2\frac{3}{2\pi}\int_{\pi/6+\alpha}^{\pi/6+\alpha+2\pi/3} V\cos(\omega t)\, d(\omega t) \\ &= \frac{3\sqrt{2}}{\pi} V_{LL}\cos\alpha \end{aligned} \tag{2-1}$$

where, V_{LL} stands for the line-to-line voltage of the AC grid and α is the firing angle of the thyristor valves.

However, if considering the DC voltage drop effected by the commutation overlap, the DC voltage expression will be correlated as :

$$V_{dcr} = \frac{3\sqrt{2}}{\pi} V_{LL} \cos\alpha - \frac{3}{\pi} \omega L_t I_{dc} \qquad (2\text{-}2)$$

where, I_{dc} is the DC current and L_t it the equivalent inductance of the tranformer.

2.2.2. LCC Inverter Modelling

The structure of the LCC inverter main circuit is the same as the LCC rectifier described in the previous section. As the firing angle α increases over 90°, the converter will operate as inverter instead, with a negative DC voltage output. Figure 2.4 shows the relationship of the firing angle with the LCC working mode [2].

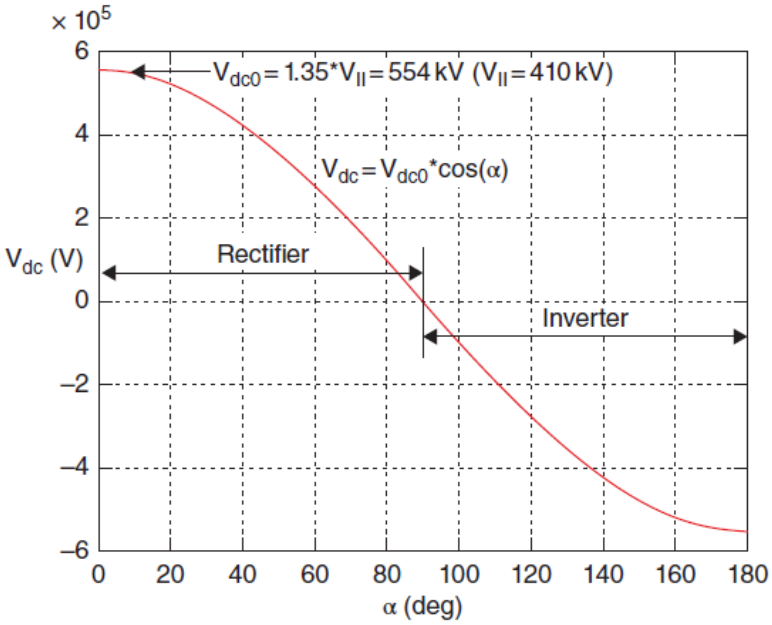

Figure 2.4 LCC DC voltage as the function of firing angle

In inverter mode, i.e. when the firing angle $\alpha > 90°$, the ignition advanced angle $\beta = 180° - \alpha$ is introduced, and the inverter DC voltage equation can be expressed similarly to the DC voltage equation of rectifier as [9]:

$$V_{dci} = \frac{3\sqrt{2}}{\pi} V_{LL} \cos\beta + \frac{3}{\pi} \omega L_t I_{dc} \quad (2\text{-}3)$$

2.2.3. AC Filters for LCC HVDC

The AC filters are designed both for the compensation of reactive power consumption of the LCC and to damp AC harmonics [11]. The power factor and reactive power consumption of the LCC can be calculated based on its working status with the method proposed in the previous section. Here, the AC filter is designed for rated DC power transmission in order to balance the reactive power under the nominal operation.

The secondary side of transformers for each 12-pulse converters have ***Y*** and ***Δ*** connection to cancel $6n^{th}$ order harmonics. The high-frequency harmonics in the AC current can be analyzed by combining the harmonic components in ***Y*** and ***Δ*** windings:

The AC current for the 6-pulse converter bridge connected to ***Y/Y*** transformer can be expressed as:

$$I_g = \frac{2\sqrt{3} I_{dc}}{\pi} \left[\sin(\omega t) - \frac{1}{5}\sin(5\omega t) + \frac{1}{7}\sin(7\omega t) - \frac{1}{11}\sin(11\omega t) + \frac{1}{13}\sin(13\omega t) \ldots \right] \quad (2\text{-}4)$$

where I_g is the line-to-line current at the primary winding of the transformer.

While, the AC current for the converter connected to ***Y/Δ*** transformer can be expressed as:

$$I_g = \frac{2\sqrt{3} I_{dc}}{\pi} \left[\sin(\omega t) + \frac{1}{5}\sin(5\omega t) - \frac{1}{7}\sin(7\omega t) - \frac{1}{11}\sin(11\omega t) + \frac{1}{13}\sin(13\omega t) \ldots \right] \quad (2\text{-}5)$$

Combining equation (2-4) and (2-5), 11^{th} and 13^{th} harmonics can only be expected in LCC side AC current if ignoring the harmonics with the order higher than 13. Thus, the AC filters are designed aiming at damping the 11^{th} and 13^{th} harmonics while compensating for the reactive power. Two single tuned AC filters are adopted to deal with the 11^{th} and 13^{th} harmonics respectively [12]. And the structure of the single tuned AC filter can be seen in Figure 2.5.

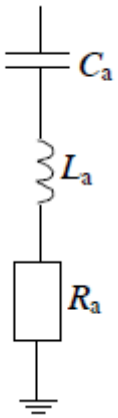

Figure 2.5 Structure of single tuned AC filter

The parameters of the single tuned filter can be calculated as [13]:

$$C_i = \frac{Q_i(N_i^2 - 1)}{\omega N_i^2 V_{LL}^2}$$
$$L_i = \frac{1}{\omega^2 N_i^2 C_i} \tag{2-6}$$

where, N_i is the AC harmonic order and Q_i is the designed reactive power under the nominal operation.

2.3. Control Scheme of LCC-HVDC

The DC current of the HVDC system is determined by the DC voltage at rectifier and inverter side, as follows [2]:

$$\mathrm{I}_{dc} = \frac{V_{dcr} - V_{dci}}{R_{dc}} \tag{2-7}$$

where R_{dc} is the total resistance of the DC cable. The DC current represents the average value under steady state. Therefore, this current can be controlled by manipulating either the DC voltage at rectifier side or the voltage at the inverter side. However, when the inverter controls DC current, there is a higher risk of commutation failure. It is more common to use the rectifier to regulate the DC current and the inverter to keep the DC voltage constant. The V-I curve with the proposed control scheme can be seen in Figure 2.6.

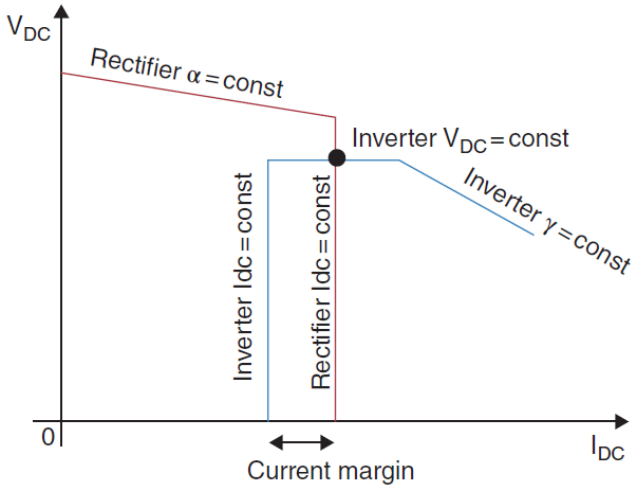

Figure 2.6 LCC-HVDC V-I operation curve

The DC voltage of the thyristor rectifier is manipulated by controlling the firing angle α as demonstrated in equation (2-8). Considering that more than one thyristor bridges can be connected in parallel to form the multi-bridge rectifier. The DC voltage can be calculated as:

$$V_{dc} = B\frac{3\sqrt{2}}{\pi}V_{LL}\cos\alpha - B\frac{3}{\pi}\omega L_t I_{dc} \tag{2-8}$$

Where, B is the number of the six-pulse bridges. Most often, B=2 or 4 as it is common to connect multiple bridges for harmonics reduction. The DC current controller of the LCC rectifier was implemented as a PI controller with the output of firing angle reference to manipulate the DC voltage of the rectifier side. The structure if the LCC rectifier controller is showed in Figure 2.7.

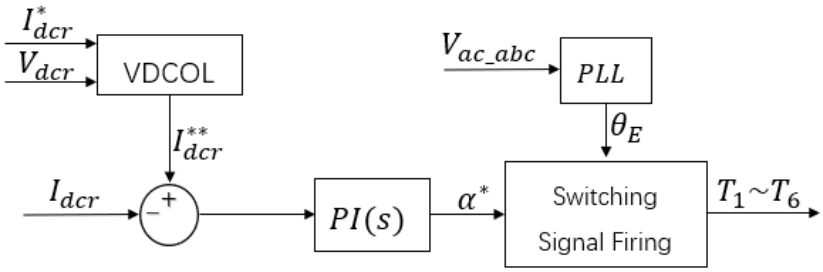

Figure 2.7 LCC rectifier DC current controller

The DC current controller of the LCC rectifier was implemented as a PI controller with the

output of firing angle reference to manipulate the DC voltage of the rectifier side based on Eq. (2-8). Besides, a voltage-dependent current order limiter (VDCOL) (see Figure 2.8) was employed to limit the current reference. With the VDCOL, the current reference will be reduced automatically when the DC voltage is reduced during disturbances [14].

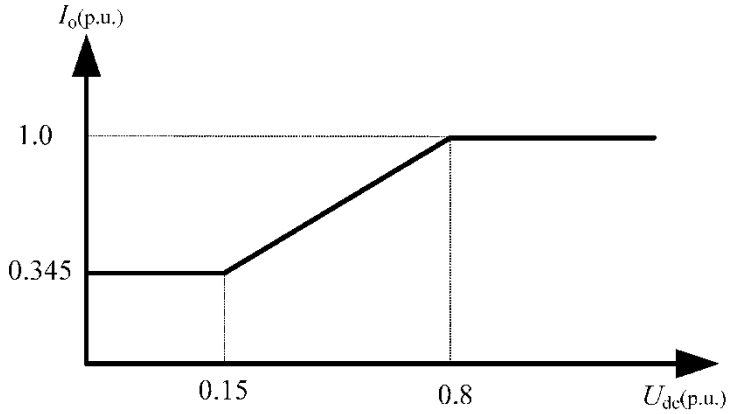

Figure 2.8 Output characteristic of VDCOL

2.3.1. LCC Inverter Controller

The principle equation for the inverter terminal is similar to the one of the rectifier:

$$V_{dc} = B\frac{3\sqrt{2}}{\pi}V_{LL}\cos\beta + B\frac{3}{\pi}\omega L_t I_{dc} \tag{2-9}$$

The primary object of the inverter control system is to maintain the DC voltage following its reference value and also to ensure a smooth operation of the system. In the inverter controller, there are three subsystems working in parallel—extinction angle (γ) control, DC voltage control and DC current margin control [2]. The minimum reference value of α generated by these three subsystems will be selected as the firing angle signal to be sent to the thyristor bridge (see Figure 2.9).

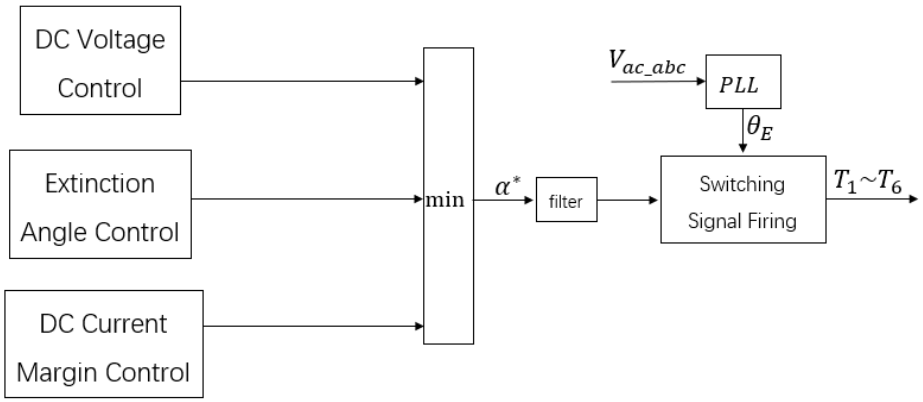

Figure 2.9 LCC inverter general control scheme

2.3.1.1. LCC Inverter Extinction Angle Control

The extinction angle γ can be estimated by introducing the extinction delay angle as [10]:

$$\cos(\delta) = \cos\alpha - \frac{I_{dc} 2\omega L_t}{\sqrt{2} V_{LL}} \tag{2-10}$$

and the extinction angle γ is defined as:

$$\gamma = 180^0 - \delta \tag{2-11}$$

As for the control of the inverter, it is important to remain safe extinction angle to prevent commutation failure. Also, try to keep the extinction angle as low as possible in order to minimize the reactive power consumption. Typically, the minimum safe extinction angle required for commutation is around 10-15^o [2]. Thus, the reference value of γ is set at 20^o to ensure safe commutation under disturbances. However, the extinction controller is always being saturated under the steady state. The structure of extinction angle control is as shown in Figure 2.10.

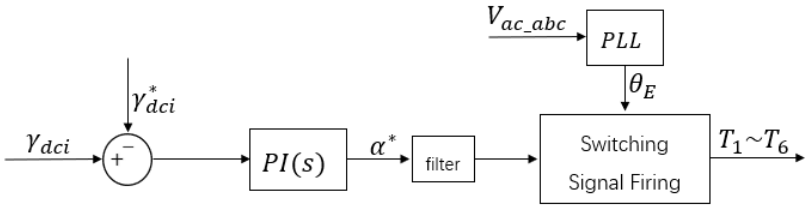

Figure 2.10 LCC inverter extinction angle control

2.3.1.2. DC Voltage Control

The DC voltage controller is usually the one being activated under the steady state. However, during the starting process or under disturbance, it can be switched into one of other two modes. Typically, the PI feedback control regulates the DC voltage tracking its reference value by changing the firing angle. The structure of the inverter DC voltage controller is shown in Figure 2.11.

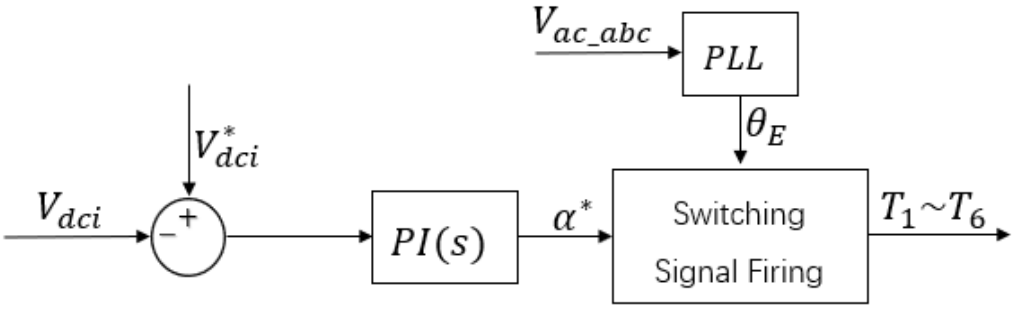

Figure 2.11 LCC inverter DC voltage control

2.3.1.3. DC Current Margin Control

The DC current control is a backup control strategy that is always saturated during normal operation. The current reference value input into the DC current control is the current reference reduced by the margin value, which always takes 10-15% of the rectifier reference current [15]. The firing angle demanded by the DC current controller is larger than the one demanded by the voltage controller. However, with the disturbances, especially during the AC grid disturbance and DC line fault, the DC current can decrease below the reference value received by the current

controller, and thus, the current controller will reduce its firing angle output to stabilize the DC current under transient.

2.4. LCC-HVDC Controller Design

The current and voltage controller parameters design of LCC-HVDC system is based on its linear model. The development of its small signal model will be explained in Chapter 4. With the state-space matrix we obtained to express the LCC-HVDC system, it can get converted into the transfer function using the following expression:

$$\mathrm{G(s)} = C(sI - A)^{-1}B + D \tag{2-12}$$

where, $\mathrm{G(s)}$ stands for the open-loop transfer function of the LCC-HVDC system connecting desired parameters, and A, B, C and D are the matrices defined with the state-space model.

The design of the controllers is aiming at regulating the DC voltage and current by manipulating the firing angles at both LCCs. Also, since the system adopts the rectifier to maintain the DC voltage and inverter to control the DC current. The open-loop transfer functions connecting I_{dc_i}-α_i and V_{dc_r}-α_r obtained from the state-space matrix are as follows:

$$G_{Ir(s)} = \frac{\Delta I_{r(s)}}{\Delta \alpha_{r(s)}} = \frac{as^2 + bs + c}{s^3 + ds^2 + es + f} \tag{2-13}$$

$$G_{Vi(s)} = \frac{\Delta V_{i(s)}}{\Delta \alpha_{i(s)}} \approx g \tag{2-14}$$

Where *a, b, c, d, e, f, g* are constants generated from the small-signal model of the LCC HVDC system.

Figure 2.12 demonstrates the structure of the rectifier with DC current PI controller:

$$G_{cc(s)} = k_p + \frac{k_I}{s} \tag{2-15}$$

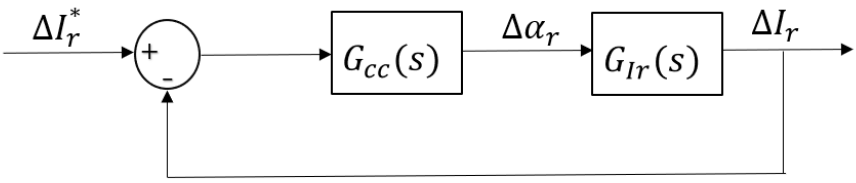

Figure 2.12 LCC-HVDC current control close-loop

And the close-loop transfer function of the system including the PI controller is:

$$\begin{aligned} G_{Ir,cc(s)} &= \frac{G_{Ir(s)}G_{cc(s)}}{1+G_{Ir(s)}G_{cc(s)}} \\ &= \frac{k_p a s^3 + (k_p b + k_i a)s^2 + (k_p c + k_i b)s + k_i c}{s^4 + (k_p a + d)s^3 + (k_p b + k_i a + e)s^2 + (k_p c + k_i b + f)s + k_i c} \end{aligned} \tag{2-16}$$

The denominator of the transfer function determines the stability of the close-loop system. This is a 4-order system where two poles can be determined by the controller's parameters and the other two remain free. Here, the pole 1 and 2 are selected to be the dominant poles of the system dynamics while pole 3 and 4 are assumed to be significantly far from the imaginary axis. Then the denominator can be reorganized as:

$$(s^2 + 2\zeta\omega_n + \omega_n^2)(s - p_3)(s - p_4) = 0 \tag{2-17}$$

where ζ stands for the damping ratio and ω_n is the natural frequency of the system. The two dominant poles can be expressed as:

$$p_{1,2} = -\zeta\omega_n \pm \omega_n\sqrt{1-\zeta^2} \tag{2-18}$$

In order to maintain the system stability, it is necessary to verify that the real part of two dominant poles should be negative. Besides, the overshoot of DC current M_p and adjustment time t_s to reach the error within 5% can be drawn from the second-order function as follows [16]:

$$M_p = 1 + e^{\frac{-\zeta\pi}{\sqrt{1-\zeta^2}}}$$
$$t_s = \frac{4}{\zeta\omega_n} \tag{2-19}$$

The close-loop transfer function of the system including the controller of DC voltage is shown in Figure 2.13.

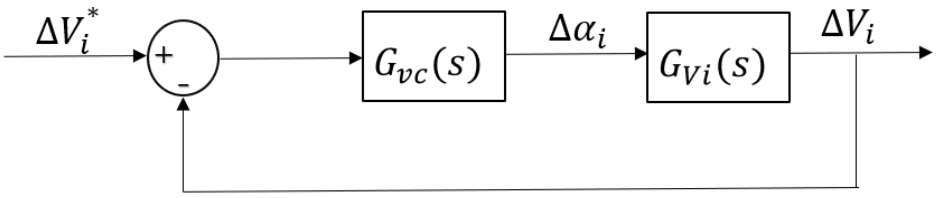

Figure 2.13 LCC-HVDC voltage control close-loop

In the design of the voltage controller, a integral controller can be used to form a first-order close-loop system.

$$G_{vc(s)} = \frac{k_i}{s} \tag{2-20}$$

And the system close loop function is:

$$G_{VI,vc(s)} = \frac{G_{VI(s)}G_{vc(s)}}{1 + G_{VI(s)}G_{vc(s)}} = \frac{1}{\frac{1}{gk_i}s + 1} \tag{2-21}$$

Then the gain of the integral controller can be calculated from a desired adjustment time τ within which DC voltage achieves 95% of the reference variation:

$$\tau = \frac{3}{gk_i} \tag{2-22}$$

Note that although only the integral gain was calculated here for the voltage controller.

However, the proportional controller is still necessary in order to compensate the errors under disturbance. Thus, a proportional controller with small gain will be added in parallel with the designed integral part to form the PI controller of DC voltage.

2.5. Non-linear Model Simulation Results for LCC-HVDC

The LCC HVDC link was modelled with MATLAB Simulink. The electric parameters for the LCCs and transformers as well as the nominal condition of the transmission system are based on the CIGRE LCC HVDC benchmark system [17][18]. The DC link was modelled using a T-equivalent model of a 200km DC cable in series connection with the DC side smoothing inductance of LCC. Also, the AC grid strength is defined with a short circuit ratio (SCR) of 5 and inductance-resistance ratio $X_L/X_R = 10$. Part of the system parameters are listed in Table 2.1.

Table 2.1 Studied LCC HVDC system Parameters

Parameters	Description	Value
f_{ac}	AC voltage frequency	50 Hz
$V_{ac(line-to-line)}$	AC grid voltage	430 kV
L_{ac}	AC grid inductance	0.0114 H
R_{ac}	AC grid resistance	0.44 Ω
V_{dc}	Rated DC voltage	500 kV
C_{dc}	DC cable capacitance	38 μF
L_{dc}	DC cable inductance	0.42 H
R_{dc}	DC cable resistance	1.9 Ω
L_{smooth}	Smoothing inductance on LCC DC terminal	0.2 H

The design of LCC controller follows the method described in section 2.4. For the LCC current

controller, the overshoot is limited to 10% of reference variation while the adjustment time is set to be $t_s = 0.2\ s$. While for the LCC voltage controller, the integral gain is calculated based on the desired adjustment time $\tau = 0.2\ s$. Also, a small proportional gain will be added to the voltage controller. The parameters of the PI controllers are listed in Table 2.2:

Table 2.2 LCC controller parameters

Gain	Value
Current Controller K_{pc}	1.50×10^{-4}
Current Controller K_{ic}	4.67×10^{-4}
Voltage Controller K_{pv}	1×10^{-6}
Voltage Controller K_{iv}	2.62×10^{-5}

The simulation result in Figure 2.14 shows the DC current injected into the DC link from the rectifier in response to the 0.5 pu step variation of its reference from nominal operation point. Also, the voltage fluctuation during the current variation was plotted in Figure 2.15.

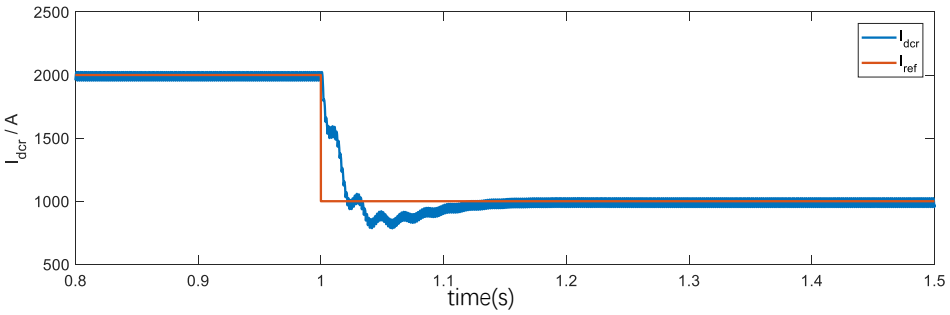

Figure 2.14 Rectifier DC terminal current of LCC-HVDC

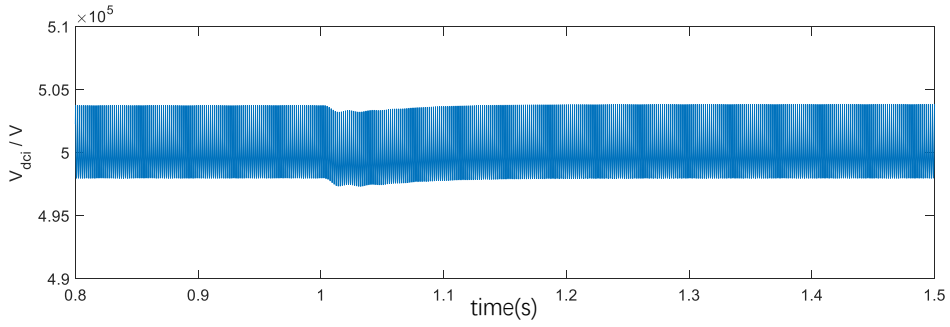

Figure 2.15 Inverter DC terminal voltage of LCC-HVDC (with low-pass filter)

Additionally, the active and reactive power at AC grid in both rectifier and inverter terminal side were plotted in Figure 2.16 and Figure 2.17. In the result, the active power difference at rectifier and inverter terminal can be considered as the power losses during the transmission, which are mainly due to the power losses of DC cable. In this case, the power losses nominal operation can be approximately weighed to be 3% of rated power. When active power is reduced, the power losses on the cable are lower. Also, the reactive power curve in Figure 2.17 showed that the reactive power consumption of both rectifier and inverter side LCC is well balanced by the AC filters during the nominal operation. However, when transmitted power reduced to half of the rated value, the reactive power is not equal to zero.

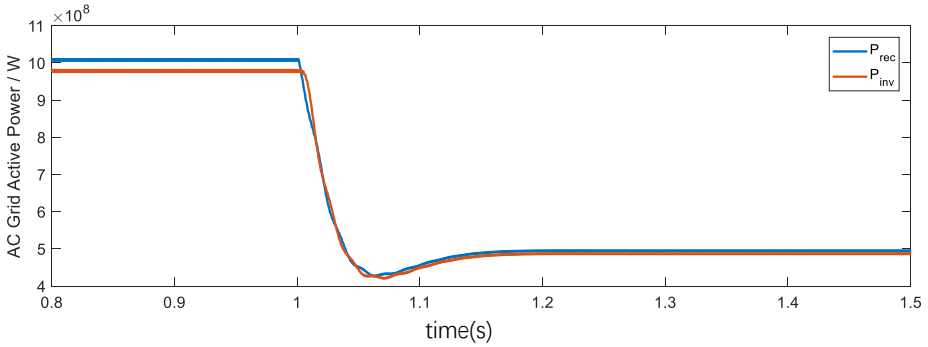

Figure 2.16 AC grid active power for LCC-HVDC (with low pass filter)

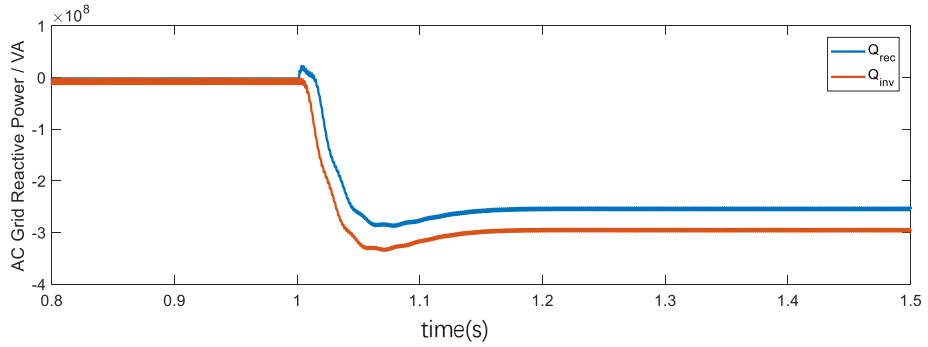

Figure 2.17 AC grid reactive power for LCC-HVDC (with low pass filter)

3. VSC-HVDC System

3.1. Introduction to VSC-HVDC

The VSC-HVDC has been an area of fast-growing interests in recent years. A VSC requires self-commutating switches which have both turn-on and turn-off capability. In most industrial applications, the voltage source converter utilizes insulated gate bipolar transistor (IGBT) for switching. In this project, a point-to-point HVDC system was modelled. Although the modular multi-level converter (MMC) represents the state of art technology of VSC with lower power losses. Considering the time limit for the thesis development, a more basic configuration, two-level VSCs were adopted in the following models. The system under analysis is sketched in Figure 3.1 [19].

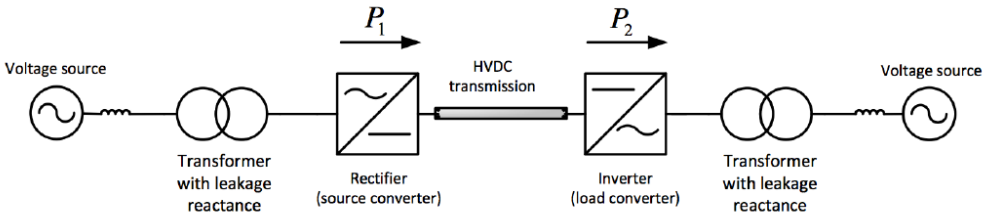

Figure 3.1 Point-to-point VSC HVDC transmission system

3.2. VSC-HVDC Modelling

The VSC composed of three branches containing two IGBT switches respectively. A simplified average model can be derived by decoupling the AC and DC side [2]. The AC side is modelled as voltage sources connecting in series with impedance (as the Thevenin equivalent of the AC grid) while the DC side is modelled as the current source in parallel with the shunt capacitor.

The current source of DC side affects the power exchanged between AC and DC side and also ensures the system power balance. The DC voltage can be expressed as the function of DC current:

$$V_{dc} = \mathrm{V}_0 + \frac{1}{C_{dc}} \int_0^t I_{dc} \tag{3-1}$$

At the AC side of a VSC, the equivalent model [2] is showed in Figure 3.2.

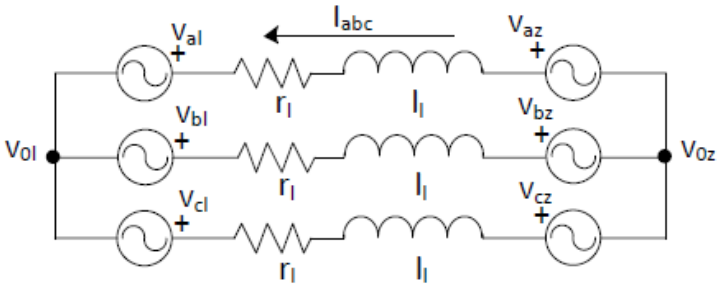

Figure 3.2 VSC equivalent model as seen from AC side

3.3. Control Scheme of VSC-HVDC

Before the implementation of the controller, it is necessary to introduce the Park transformation. This transformation turns the three-phase variables on the three-phase stationary frame (*abc*) into the two-phase synchronous reference frame (*qd*). In the synchronous *qd* frame, the active power is aligned to the q-axis current component while d-axis component is corresponding to reactive power. Using Park transformation, it is possible to design the controller with constant quantities to regulate variables on the rotary frame. More details can be found in Appendix A. Park Transformation.

The VSC control systems are designed based on rotary qd frame. Both VSCs in the system has the ability to control the active and reactive power flow independently by regulating two electrical variables in qd frame. Thus, both VSC terminals in this point-to-point connection can be used to manipulate the power flow or DC voltage. Active and reactive power in *qd* frame can be expressed as:

$$P = \frac{3}{2}(V_q I_q + V_d I_d)$$
$$Q = \frac{3}{2}(V_q I_d - V_d I_q) \tag{3-2}$$

The VSC control scheme is based on two-level cascaded controller. The inner loop controller regulates the AC grid current in dq frame while the outer loop regulates the DC voltage.

In a point-to-point VSC HVDC connection, one of the converters will be used to regulate the AC current flow while the other one to maintain the DC voltage. Although in the connection of

VSC HVDC, both rectifier and inverter can be swapped between these two controlling modes. Considering the risk of rectifier DC terminal overvoltage if using the inverter to control the DC voltage. In this thesis, the rectifier will take the general control scheme described above to regulate the DC voltage, while the inverter will only utilize the inner loop current controller to manipulate the active and reactive power injected from the DC link to the receiving end AC terminal independently.

The rectifier controller is based on two-level cascade control. In summary, the general scheme of the rectifier side VSC is showed in Figure 3.3 below.

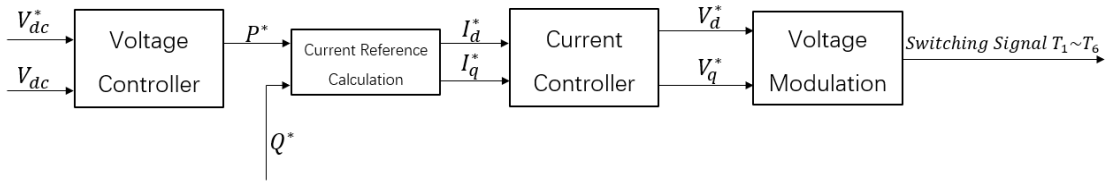

Figure 3.3 VSC rectifier general control scheme

In the control system of the VSC rectifier, the reference signal of active power is given by the voltage controller. While the reactive power can also be regulated to support the AC grid voltage. However, since the thesis is mainly focused on the DC dynamics of the transmission system. The reference signal Q^* will be simply set to a constant.

The control strategy for the inverter is to regulate the active and reactive power injected into the grid instead of DC voltage. Thus, the voltage controller is not utilized in the inverter control system [20]. The structure of the inverter controller can be seen in Figure 3.4.

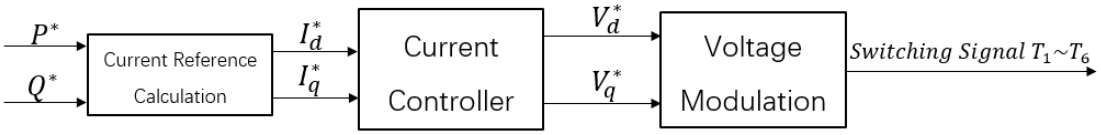

Figure 3.4 VSC inverter general control scheme

3.3.1. VSC Control System Voltage Loop

The outer loop contains the DC voltage regulator. The DC voltage controller, as shown in Figure 3.5, is required to keep the DC voltage stable at its reference value by ensuring the

balance between the power feed into the DC link and the power injected into the AC grid. The DC voltage regulator adopts PI controller with the input signal of measured DC voltage and its reference value. The output of the controller is the reference value of active power.

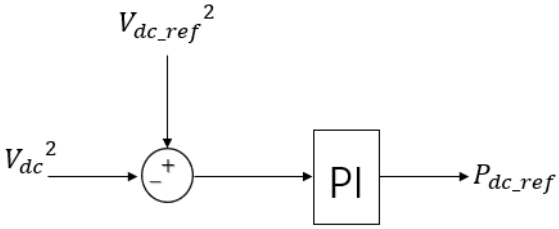

Figure 3.5 VSC DC voltage controller

With the reference value of power, the current reference can be obtained through simple calculation:

$$\begin{aligned} i_q^* &= \frac{2}{3}\frac{P^*}{V_{acq}} \\ i_d^* &= \frac{2}{3}\frac{Q^*}{V_{acq}} \end{aligned} \tag{3-3}$$

Note that when the AC grid voltage is transformed into *qd* frame, the d-axis component is supposed to be zero under steady state. Here, in the rectifier, since the DC voltage is balanced by regulating the active power follow. Only the reference current i_q^* is required to be modified according to the real-time measurement of DC voltage. The reactive power can be controlled by regulating i_d^*.

According to the reference[20], the close-loop transfer function of the voltage PI controller can be formed as eq.(3-4).

$$\frac{V_{dc}{}^2(s)}{V_{dc}^{*2}(s)} = \frac{2s\xi_E\omega_E + \omega_E^2}{s^2 + 2s\xi_E\omega_E + \omega_E^2} \tag{3-4}$$

where, ξ_E is the damping ratio of voltage loop and ω_E is the desired angular velocity of voltage loop. Thus, the PI controller gains can be defined as:

$$\begin{aligned} K_P &= C\xi_E\omega_E \\ K_I &= \frac{C\omega_E^2}{2} \end{aligned} \tag{3-5}$$

Similar to the LCC voltage design described in section 2.4 that the overshoot of DC voltage M_p and adjustment time t_s to reach the error within 5% can be drawn from the second-order system:

$$M_p = 1 + e^{\frac{-\zeta\pi}{\sqrt{1-\zeta^2}}}$$
$$t_s = \frac{4}{\zeta\omega_n} \tag{3-6}$$

3.3.2. VSC Control System Current Loop

The current reference was sent to the current controller. The current controller decouples the *d* and *q* components of voltage and current according to the following eqaution [20]:

$$\begin{bmatrix} V_q^* \\ V_d^* \end{bmatrix} = \begin{bmatrix} r_l & 0 \\ 0 & r_l \end{bmatrix} \begin{bmatrix} i_q \\ i_d \end{bmatrix} + \frac{d}{dt} \begin{bmatrix} l_l & 0 \\ 0 & l_l \end{bmatrix} \begin{bmatrix} i_q \\ i_d \end{bmatrix} \tag{3-7}$$

Accordingly, our current controller is sketched in Figure 3.6:

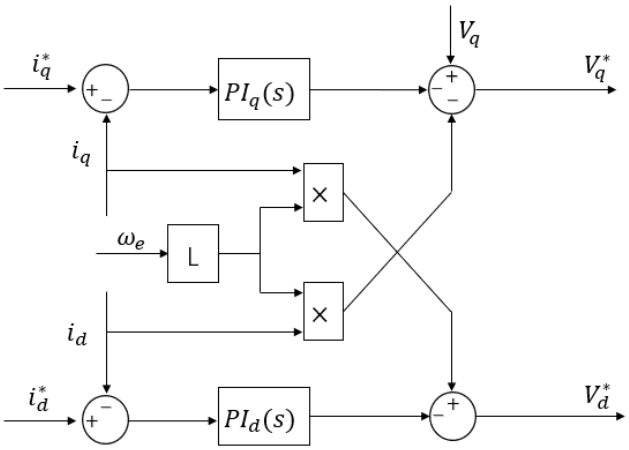

Figure 3.6 VSC AC current controller

The current controller is designed using Internal Model Control Technique [21]:

$$K_P = \frac{l_l}{\tau}$$
$$K_I = \frac{r_l}{\tau} \tag{3-8}$$

where, l_l and r_l stand for the inductance and resistance of the VSC connected AC grid respectively

3.3.3. PWM in VSC Control System

With the reference value of voltage, the inverse Park transformation of the *qd* components can be used to get the voltage reference in *abc* frame V^*_{abc}. The voltage reference will be sent to the voltage modulation block to generate the switching signals of six pulse IGBT bridge. Here, in the switching signal generating module, the Pulse Width Modulation (PWM) is adopted. With PWM, the switching signal with variable pulse width is modulated by comparing the reference voltage signal and high-frequency triangular carrier wave as shown in Figure 3.7.

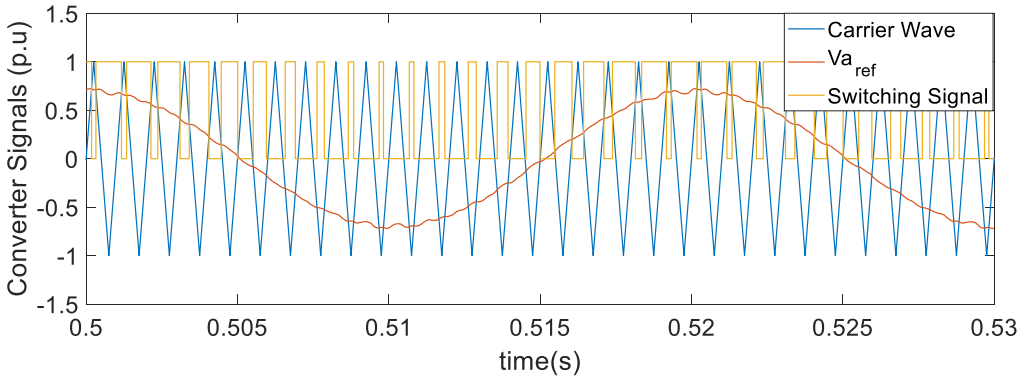

Figure 3.7 PWM switching signal generating

Besides, the Phase Lock Loop (PLL) is needed to track the angular position by estimating the rotary velocity of the AC grid voltage (see subsection 3.3.4).

3.3.4. Phase Lock Loop

The PLL is used to give the reference signal for the converter controller to synchronize with the AC voltage by estimating the electrical angle and its angular velocity. A three-phase PLL consists of a PI control with the feedback of *d*-axis voltage component. The output of the controller is the angular velocity of the electrical system ω_e. The electrical angle ω_e can be obtained from the integration of the angular velocity. The control system of PLL is shown in

Figure 3.8.

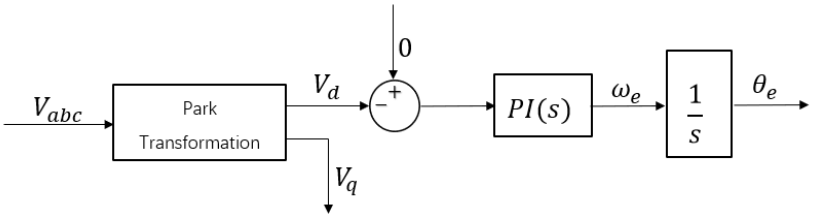

Figure 3.8 Scheme of PLL control system

3.4. VSC-HVDC Non-Linear Model Simulation Results

The VSC HVDC network was modelled with MATLAB Simulink. The electric parameters for the VSCs as well as the nominal condition of the transmission system is based on the CIGRE VSC HVDC benchmark system [22]. The DC link was modelled using a T-equivalent model of a 200km DC cable. The AC grid is defined with a short circuit ratio of 5 and inductance-resistance ratio $X_L/X_R = 10$. Part of the system parameters are listed in the following table:

Table 3.1 Parameters set for VSC HVDC model

Parameters	Description	Value
f_{ac}	AC voltage frequency	50 Hz
$V_{ac(line-to-line)}$	AC grid voltage(rms)	220 kV
R_{ac}	AC grid resistance	0.26 Ω
L_{ac}	AC grid inductance	6.6 mH
V_{dc}	Rated DC voltage	500 kV
C_{dc}	DC cable capacitance	38 μF
L_{dc}	DC cable inductance	0.42 H
R_{dc}	DC cable resistance	1.9 Ω

The simulation results in Figure 3.9 and Figure 3.10 of the VSC HVDC model shows the rectifier side DC voltage and the AC current in inverter terminal with *d* and *q*-axis component respectively in response to a 0.5 pu step variation of the current reference from their nominal operating point. The AC grid current curve shows that q and d axis component is fully decoupled. Thus the active and reactive power can be regulated independently using the VSC. Also, I_{qi} does not strictly follow the desired first-order curve due to the interaction of DC cable.

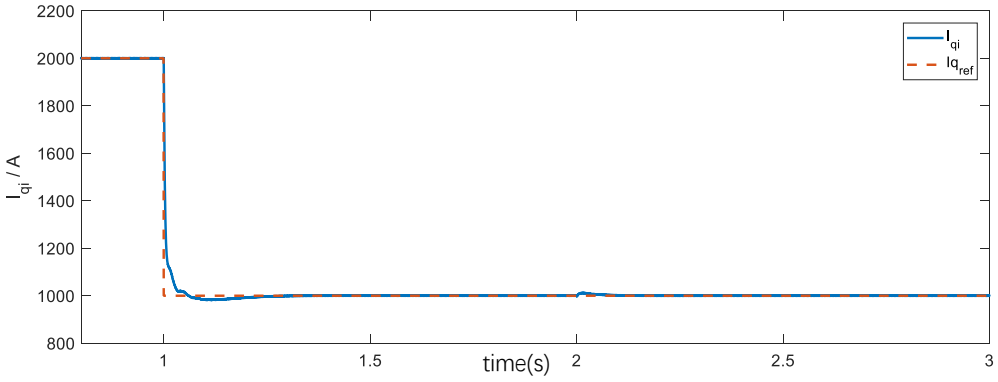

Figure 3.9 Inverter AC terminal q-axis current VSC-HVDC

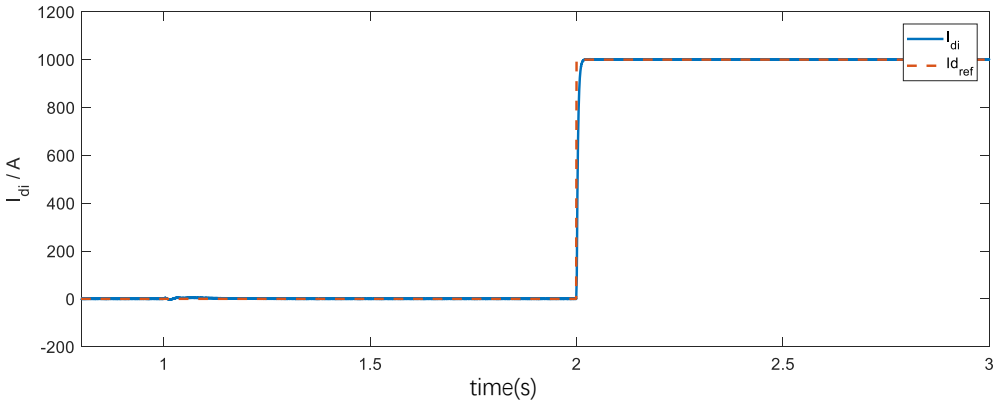

Figure 3.10 Inverter AC terminal d-axis current VSC-HVDC

Also, the AC current in rectifier terminal with *q* and *d*-axis component are plotted below in Figure 3.11 and Figure 3.12. Note that the q-axis current in rectifier shows the same trend as I_{qi} under the manipulation of rectifier controller in order to maintain the DC voltage by balancing the active power flow into the DC link.

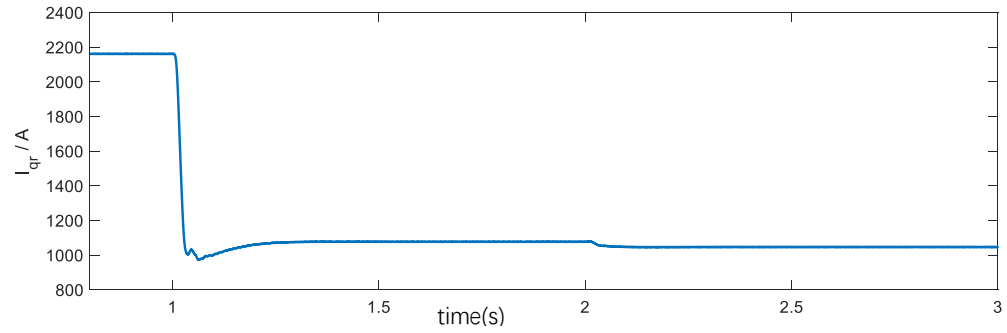

Figure 3.11 Rectifier AC terminal q-axis current VSC-HVDC

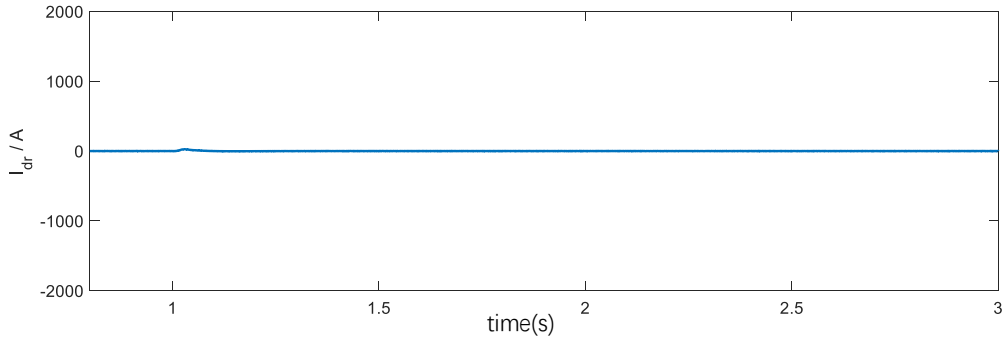

Figure 3.12 Rectifier AC terminal d-axis current VSC-HVDC

Accordingly, the rectifier DC terminal voltage in response to the current variation can be seen in Figure 3.13. The rectifier controller adopts the principle that the fluctuation of DC voltage should always within the range of $\pm 10\%$ nominal value.

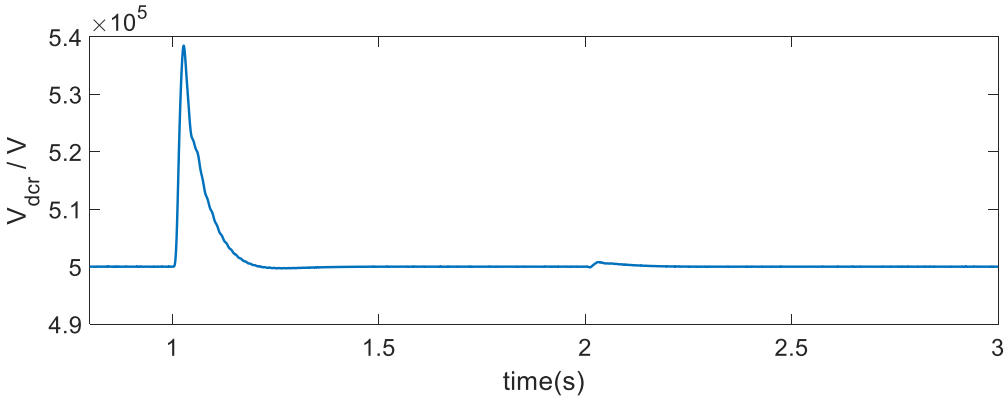

Figure 3.13 Rectifier DC terminal voltage of VSC-HVDC

Besides, the active and reactive power at each AC grid corresponding to the current variation were plotted in Figure 3.14 and Figure 3.15. The difference between of active power transmitted

in both converters is approximately 70 MW under nominal operation which is mainly due to the power losses on the DC cable and two converters.

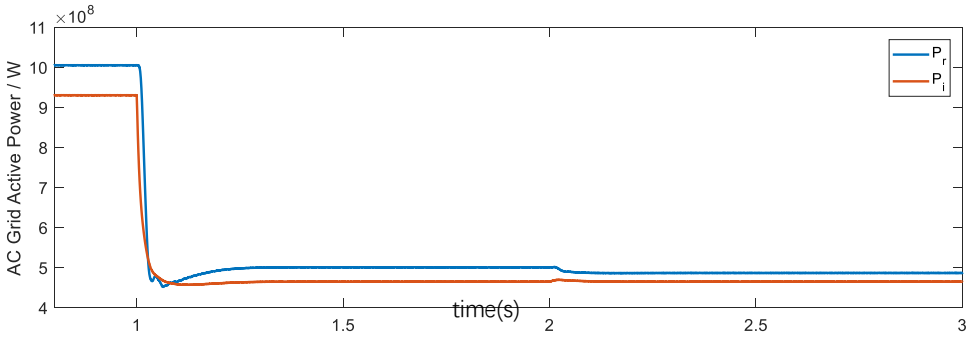

Figure 3.14 AC Grid active power for VSC-HVDC

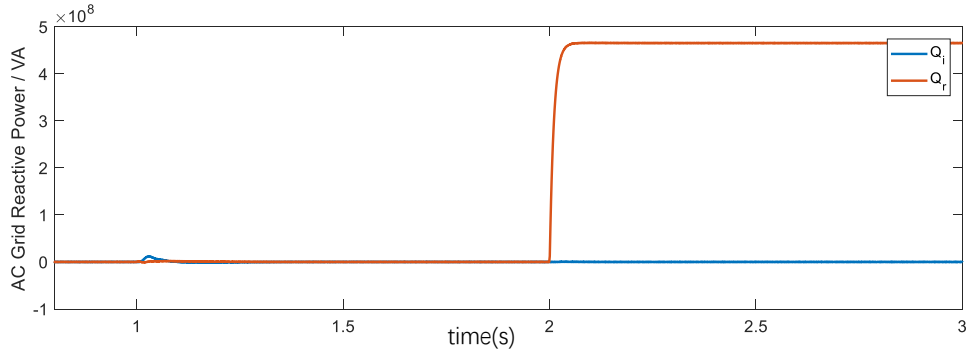

Figure 3.15 AC Grid reactive power for VSC-HVDC

4. Hybrid LCC-VSC HVDC

Based on the previous study on the LCC and VSC HVDC system, the basics of hybrid LCC-VSC HVDC transmission system is analyzed in this chapter. Point-to-point hybrid LCC-VSC HVDC connection models were built using MATLAB Simulink combining CIGRE benchmark model of LCC-HVDC and VSC-HVDC.

In the hybrid transmission system, either rectifier or inverter terminal can adopt the LCC topology while another one adopts VSC topology. Also, each terminal may have the controlling object of DC voltage or current/power. Thus, four different configurations (see Table 4.1) should be taken into consideration while modelling the basic hybrid HVDC system.

Table 4.1 Optional configurations of hybrid VSC-LCC HVDC

	Notation	Rectifier Terminal	Inverter Terminal
Configuration 1	$LCC_v - VSC_i$	LCC, controls DC voltage	VSC, controls AC current
Configuration 2	$LCC_i - VSC_v$	LCC, controls DC current	VSC, controls DC voltage
Configuration 3	$VSC_v - LCC_i$	VSC, controls DC voltage	LCC, controls DC current
Configuration 4	$VSC_i - LCC_v$	VSC, controls AC current	LCC, controls DC voltage

The structure of the hybrid HVDC connection as well as the control schemes can be seen in Figure 4.1 and Figure 4.2.

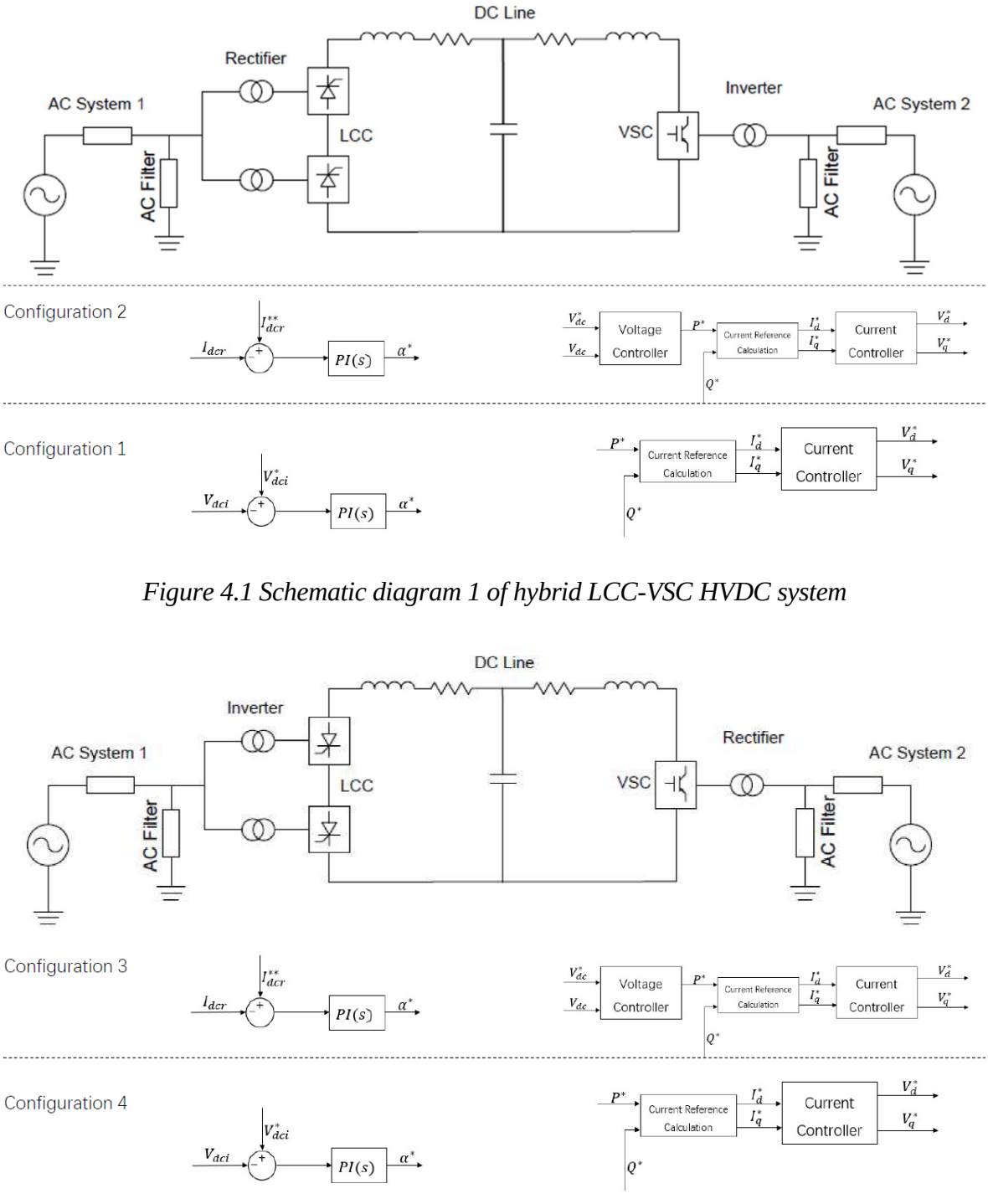

Figure 4.1 Schematic diagram 1 of hybrid LCC-VSC HVDC system

Figure 4.2 Schematic diagram 2 of hybrid LCC-VSC HVDC system

The design of both LCC and VSC controllers follows the method proposed for the LCC-HVDC and VSC-HVDC control system as described in the previous chapters.

Generally, in order to ensure the system stability, the VSC controller will be designed to have faster dynamics compared to the LCC controller. Considering the starting-up process, all the four configurations can use VSC for pre-charging but only the two configurations with LCC as the rectifier terminal are able to start with the LCC.

4.1. Starting-Up Strategy of Hybrid HVDC System

The starting process of the hybrid HVDC transmission system includes two stages: pre-charging of the system and ramping up to the nominal operating point with the controllers activated.

During the pre-charging process, one of two converter terminals is supposed to work as passive diode bridge to establish the DC voltage while the other one keeps blocked to avoid power flow between AC and DC grid over the converter terminal. In configuration 1 and 2, as mentioned in the previous section, both LCC and VSC can be used to complete the pre-charging of the DC network. However, in configuration 3 and configuration 4, since the LCC with inverter mode is not able to provide the pre-charging current by reversing the power flow, only VSC at rectifier side can be used to initialize the DC voltage. The starting process with VSC and LCC pre-charging is described as subsections 4.1.1 and 4.1.2:

4.1.1. VSC Pre-charging

The operation sequence for the pre-charging process using the VSC is listed as follows:

1. Both converters are blocked.
2. Unblock VSC to ramp up DC voltage.
3. Once the DC voltage achieves the target value, the DC voltage controller at VSC is activated. Also, bypass the current limiting resistors (if any).
4. Activate the LCC controller.

4.1.2. LCC Pre-charging

The operation sequence for the pre-charging process using the LCC rectifier is listed as following [23]:

1. Both converters are blocked.

2. LCC rectifier is unblocked. A fixed reference firing angle α^* is given to the rectifier to ramp up the DC voltage

3. Once the DC voltage reaches the target value, the LCC and VSC voltage controllers are activated at the same time. Also, bypass the current limiting resistors (if any).

4.2. Simulation Results of The Hybrid Non-Linear Model

In this section, the simulation results including the completed starting-up process of each hybrid configurations were plotted to validate the proposed operation strategy in following Figure 4.3 to Figure 4.7. For all the configurations, the system will be started to the nominal condition and then reduce the current to 0.5 pu.

In configuration 1 of $LCC_v - VSC_i$, VSC precharging was deployed. Thus the pre-charging current can be found in the VSC side AC grid q-axis current. After the precharging finished, the voltage controller of the LCC will be activated while the VSC is regulated to control the AC current. For all of four configurations, the difference in active power is the power losses over the DC cable and both converters. From the reactive power, it can be observed that the reactive power is equal to zero with nominal current in both rectifier and inverter side since the AC filters are designed to balance the reactive power under nominal condition. However, the reactive power will not be zero with the reduced current.

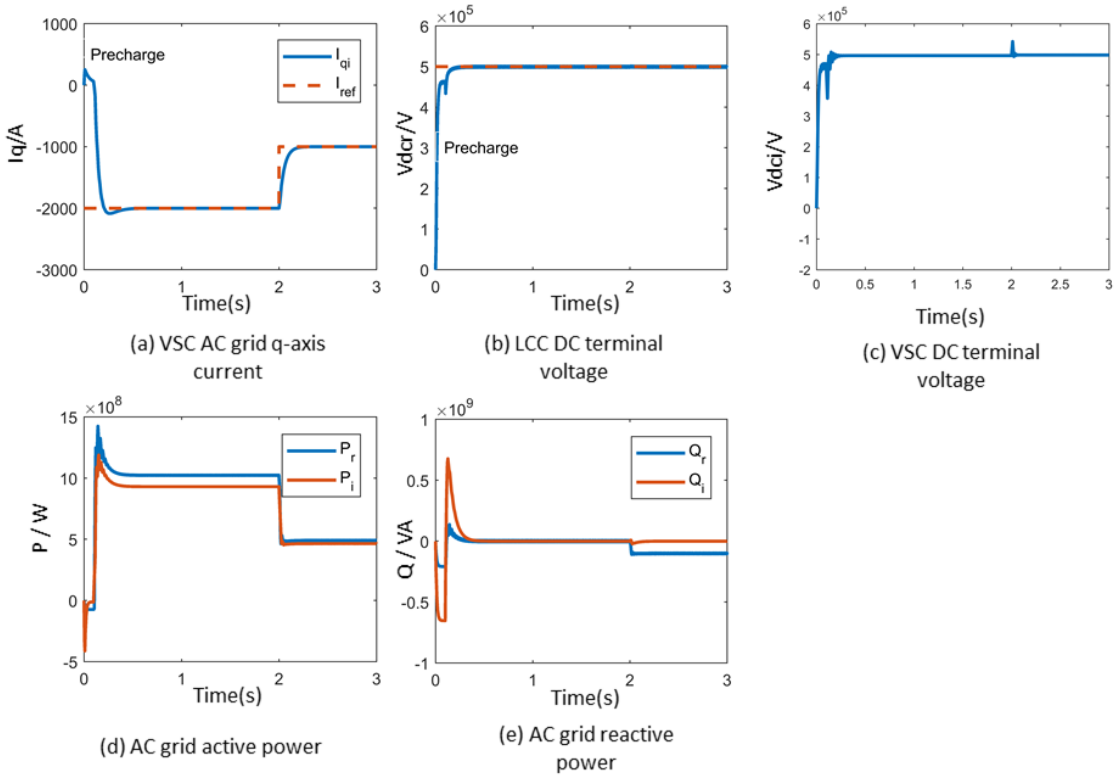

Figure 4.3 Result of hybrid HVDC system LCC_v-VSC_i with VSC precharging

In configuration 2 of $LCC_i - VSC_v$, the results of the simulation that adopts LCC and VSC for starting-up are plotted in Figure 4.4 and Figure 4.5 respectively. From the simulation results, both starting-up strategies can be verified. Also, compared to configuration 1, the DC current dynamics is slower due to the difference between LCC and VSC.

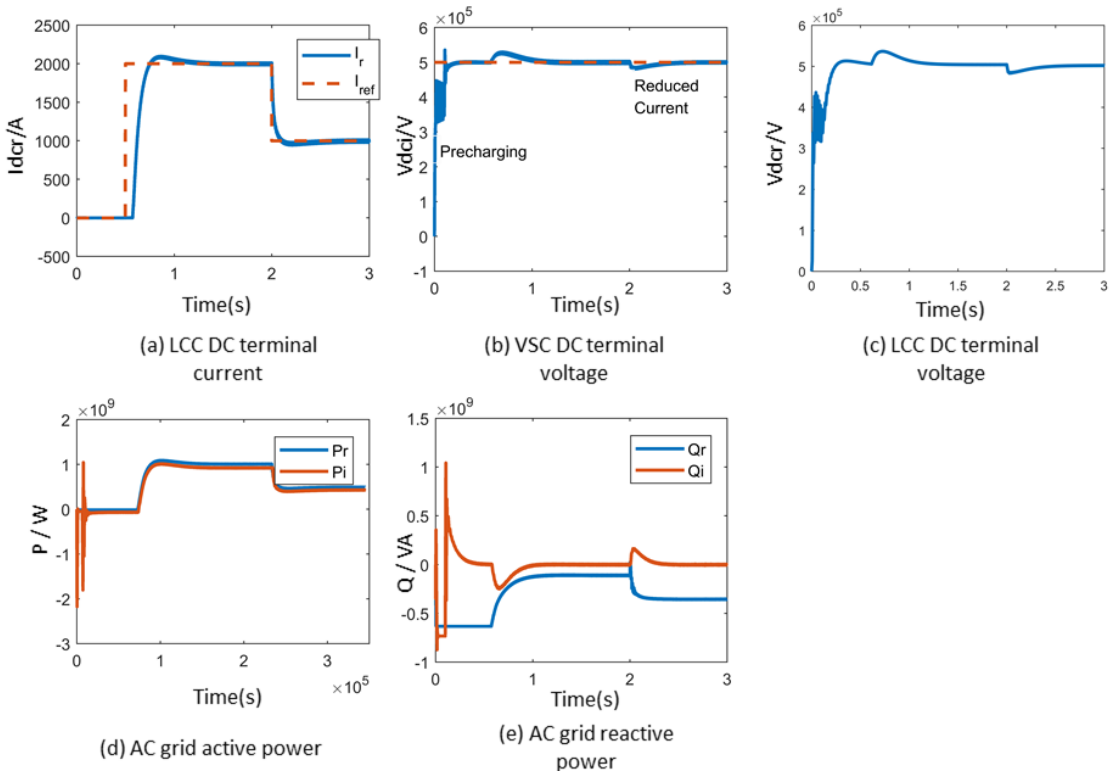

Figure 4.4 Result of hybrid HVDC system LCC_i-VSC_v with VSC preecharging

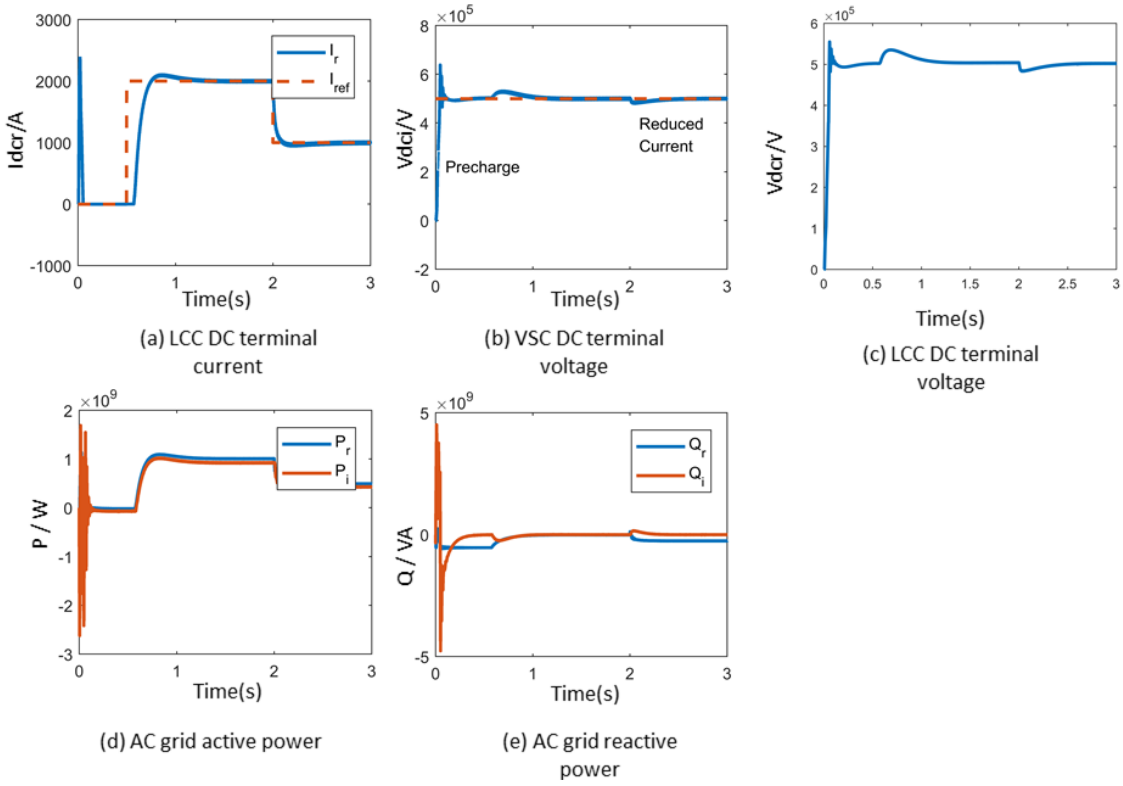

Figure 4.5 Result of hybrid HVDC system LCC_i-VSC_v with LCC preecharging

Configuration 3 $VSC_v - LCC_i$ is only allowed to pre-charge the DC link with VSC. Once the DC voltage is established by VSC pre-charging, the voltage controller of VSC will be activated to ramp up the DC voltage reaching its rated value. Then, the DC current will be regulated under the control of LCC terminal. The dynamics of DC voltage and current is quite similar to configuration 2 $LCC_i - VSC_v$ since their control strategy is the same despite of difference in converters working mode. However, this configuration is more stable because LCC is not operating as the inverter, thus, the risk of commutation failure reduced.

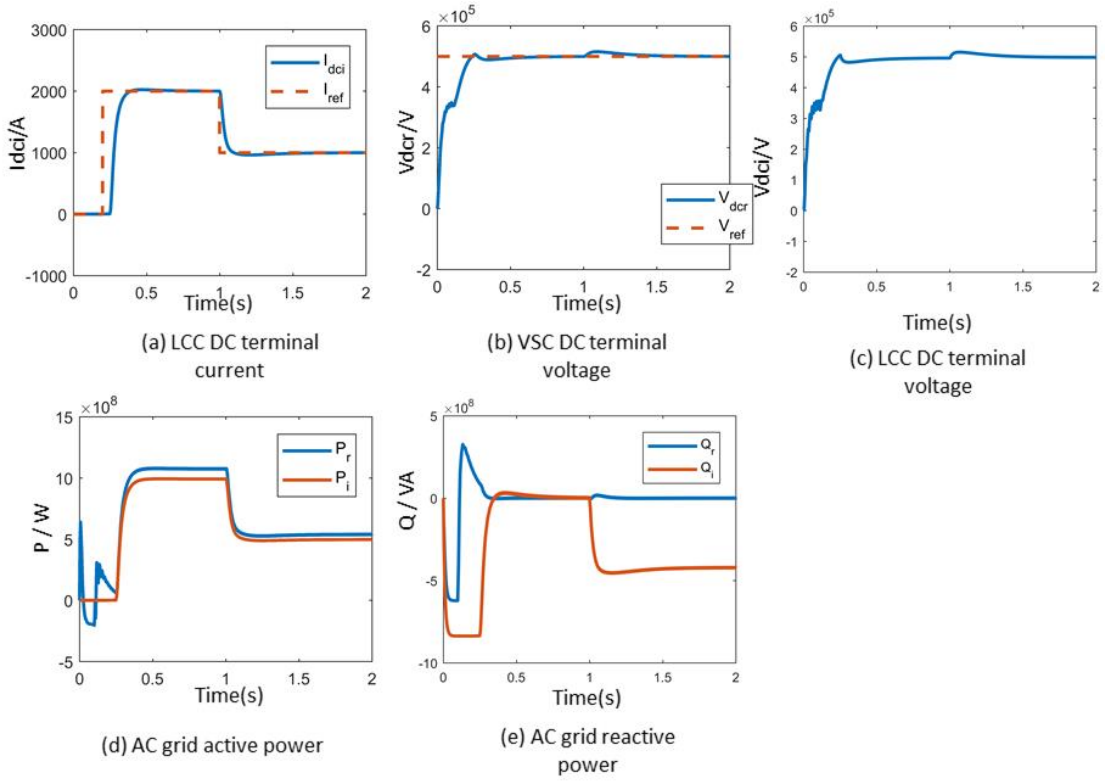

Figure 4.6 Result of hybrid HVDC system VSCv-LCCi with VSC preecharging

Configuration 4 $VSC_i - LCC_v$ is also adopting VSC for pre-charging the system. And the result of this configuration in Figure 4.7 shows similar dynamics as configuration 1 $LCC_i - VSC_v$. Also, the risk of LCC commutation failure is lower than in configuration 1.

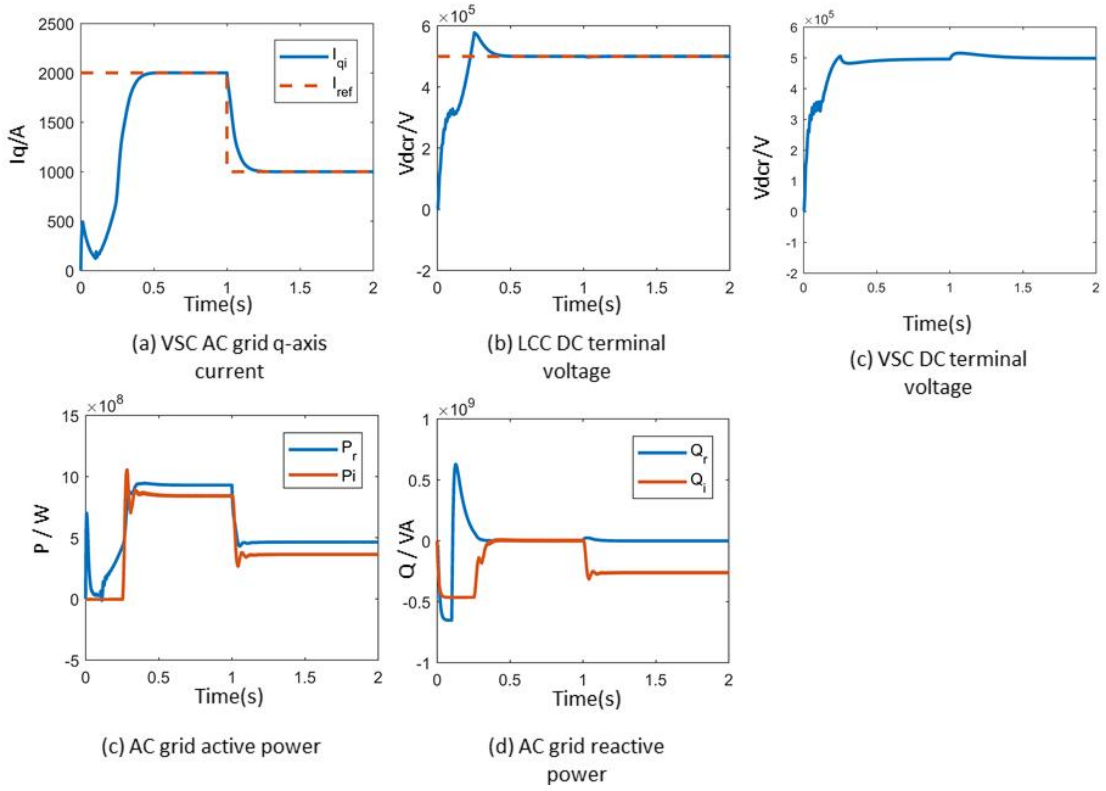

Figure 4.7 Result of hybrid HVDC system VSCi-LCCv with VSC preecharging

4.3. Comparison of Four Hybrid HVDC Configurations

From the modelling and simulation of the hybrid LCC-VSC HVDC system, some conclusions can be drawn in this chapter.

4.3.1. Configuration1: LCC_v-VSC_i

Configuration 1 built for the hybrid HVDC system adopts the LCC for the rectifier and VSC for the inverter. The LCC controls the DC voltage and VSC regulates the DC current. With this topology and operation mode, the inverter terminal with VSC is able to make the fast response to the load variation in receiving side AC grid. Also, with the VSC, the transmission system has the potential to be connected to the weak grid or passive grid. However, since the dynamic response of LCC is much slower than VSC, LCC may not able to follow the VSC current/power regulation during the transient, which will result in a large fluctuation in DC voltage.

4.3.2. Configuration 2: LCC_i-VSC_v

In configuration 2 of hybrid HVDC connection, VSC of the receiving end regulates the DC

voltage. Compare to configuration 1, this kind of operation strategy is more stable in DC voltage. On the other hand, the DC current/power response controlled by LCC is slower.

For the starting process of this configuration, similar to configuration 1, the VSC capacitor can be pre-charged either by the rectifier side LCC or the VSC inverter itself. Except for the pre-charging process, the performance of the controller during normal operation is still the same.

4.3.3. Configuration 3: VSC_v-LCC_i

In configuration 3, the VSC at rectifier terminal regulates the DC voltage while the LCC at inverter terminal controls the DC current. Similar to configuration 1, since the dynamical response of the LCC is much slower than VSC, LCC may not follow the VSC current/power regulation during the transient, which will result in the large fluctuation in DC voltage. Due to the DC current operation in the LCC terminal, this configuration presents the highest risk of commutation failure.

4.3.4. Configuration 4: VSC_i-LCC_v

Configuration 4 adopts VSC at the rectifier terminal and LCC at the inverter terminal while VSC regulates the DC current and LCC controls the DC voltage. This kind of configuration is suitable for the connection of renewable power plant, especially the offshore wind farm. The VSC can regulate active and reactive power independently of the offshore grid while saving the space on the offshore platform comparing to the application with LCC. The power losses at the receiving end are minimized due to the utilization of LCC. However, similar to configuration 1, since the dynamical response of LCC is slower than VSC, the fluctuation in DC voltage will occur when current reference changes at VSC side.

5. Small-Signal Model Analysis of Hybrid HVDC

5.1. Small-signal Model of Hybrid HVDC

Small-signal model is an important method where the mathematical model will be linearized. Small-signal model based stability analysis can be a tool in the design stage of HVDC controller to enhance their resilience to fault, and to improve their ability to contribute to power network operation [24]. Besides, with the linearized result of the hybrid HVDC system, the potential interactions between converters can be investigated [25][26]. Based on the small-signal model, the eigenvalue analysis can be conducted to study the system stability, dynamics and the potential influence of system state elements.

With the small signal model, the complete system function can be organized and expressed in the state-space matrix form:

$$\begin{aligned} \dot{X} &= AX + BU \\ Y &= CX + DU \end{aligned} \tag{5-1}$$

where X is the state vector of the system, Y is the output vector, U stands for the input vector. And A, B, C, D are the matrix corresponding to the system parameters.

Also, the eigenvalue matrix can be calculated by solving the characteristic equation [27]:

$$\det(A - \lambda I) = 0 \tag{5-2}$$

where the n solutions of $\lambda=\lambda_1, \lambda_2, ..., \lambda_n$ are eigenvalues of A. For any eigenvalue, the right eigenvector ϕ is defined by the following expression:

$$\mathrm{A}\phi = \lambda\phi \tag{5-3}$$

Similarly, the left eigenvalue vector is defined as the solution ψ of :

$$\psi\mathrm{A} = \psi\lambda \tag{5-4}$$

Based on the results above, the relationship between the states and the modes can be indentified with the participation factor matrix [27]:

$$P = \psi * \phi^T \tag{5-5}$$

5.1.1. Small-signal Model of AC Grid

The AC grids connected in both rectifier and inverter side are modelled as their Thevenin equivalent circuit. The linearization of the AC grid elements is deployed in the synchronous *q-d* frame.

Since the mathematical model of the VSC and LCC are different, the small-signal model of the AC grid in the VSC side and LCC side are organized in two different structures:

5.1.1.1. Small-signal Model of VSC AC Grid

As the Thevenin equivalent circuit showed in Figure 5.1, AC grid connected by the VSC can be modelled with two voltage sources including the influence of AC grid impedance and AC filter capacitor.

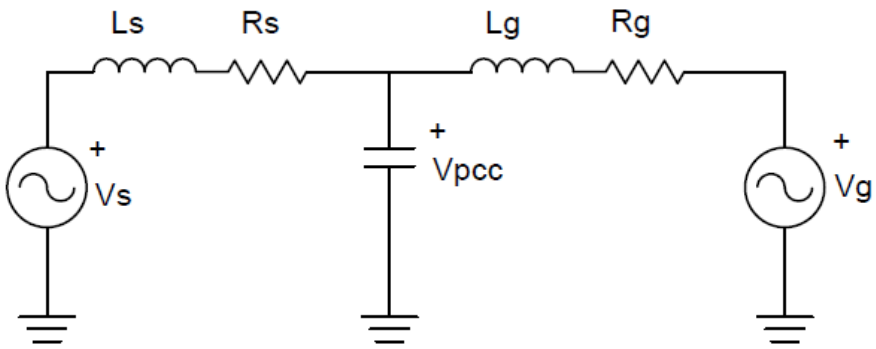

Figure 5.1 VSC AC grid equivalent single line circuit

In the small-signal model of VSC-HVDC, the voltage at the point where the converter terminal is connected with the AC grid is generated directly by the VSC under the manipulation of its control system. And the voltage (in *q-d* frame) can be used as the input of the AC grid small-signal model. The states of the linear model are selected as the AC grid current and voltage of the point of common coupling (PCC). Small-signal model of VSC side AC grid with state-space matrix expression can be seen as:

$$\begin{bmatrix} \Delta\dot{I}_d \\ \Delta\dot{I}_q \end{bmatrix} = \begin{bmatrix} -R_s/L_s & \omega_e \\ -\omega_e & -R_s/L_s \end{bmatrix} \begin{bmatrix} \Delta I_d \\ \Delta I_q \end{bmatrix} + \begin{bmatrix} -1/L_s & 0 \\ 0 & -1/L_s \end{bmatrix} \begin{bmatrix} \Delta V_d \\ \Delta V_q \end{bmatrix}$$
$$\begin{bmatrix} \Delta I_d \\ \Delta I_q \\ \Delta V_{pcc\_d} \\ \Delta V_{pcc\_q} \end{bmatrix} = \begin{bmatrix} 1 & 0 \\ 0 & 1 \\ -R_g & -\omega_e L_g \\ \omega_e L_g & -R_g \end{bmatrix} \begin{bmatrix} \Delta I_d \\ \Delta I_q \end{bmatrix} \quad (5\text{-}6)$$

5.1.1.2. Small-signal Model of LCC AC Grid

Due to the differences of the operation principle between VSC and LCC, the AC terminal of LCC is supposed to be modelled as a current source with the magnitude according to the power flow between the AC grid and DC link. The equivalent circuit of LCC connected AC grid circuit is showed in Figure 5.2.

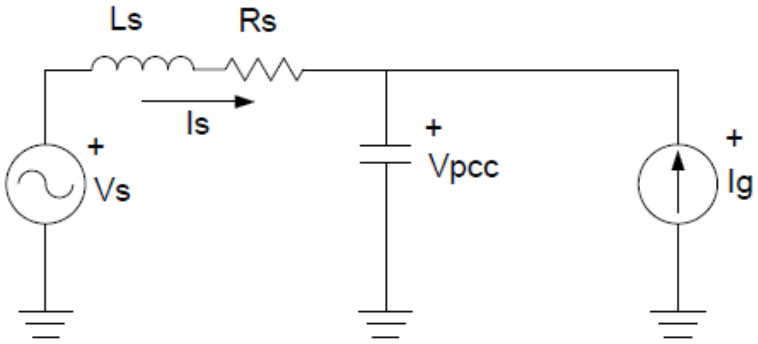

Figure 5.2 LCC AC grid equivalent single line circuit

In the small-signal model of LCC side AC grid, the input of the state-space model, instead of the converter voltage, should be the current in *q-d* frame. The current can be obtained from the power balance in the AC-DC interface of LCC. The AC grid of LCC side can be linearized as the following state-space system:

$$\begin{bmatrix} \dot{I}_{sd} \\ \dot{I}_{sq} \\ \dot{V}_{gd} \\ \dot{V}_{gq} \end{bmatrix} = \begin{bmatrix} -R_s/L_s & -\omega_e & -1/L_s & 0 \\ \omega_e & -R_s/L_s & 0 & -1/L_s \\ 1/C_{ac} & 0 & 0 & -\omega_e \\ 0 & -1/C_{ac} & -\omega_e & 0 \end{bmatrix} \begin{bmatrix} I_{sd} \\ I_{sq} \\ V_{gd} \\ V_{gq} \end{bmatrix} + \begin{bmatrix} 0 & 0 & 1/L_s & 0 \\ 0 & 0 & 0 & 1/L_s \\ -1/C_{ac} & 0 & 0 & 0 \\ 0 & -1/C_{ac} & 0 & 0 \end{bmatrix} \begin{bmatrix} I_{gd} \\ I_{gq} \\ V_{sd} \\ V_{sq} \end{bmatrix} \quad (5\text{-}7)$$

$$\begin{bmatrix} I_{sd} \\ I_{sq} \\ V_{gd} \\ V_{gq} \end{bmatrix} = \begin{bmatrix} 1 & 0 & 0 & 0 \\ 0 & 1 & 0 & 0 \\ 0 & 0 & 1 & 0 \\ 0 & 0 & 0 & 1 \end{bmatrix} \begin{bmatrix} I_{sd} \\ I_{sq} \\ V_{gd} \\ V_{gq} \end{bmatrix}$$

5.1.2. AC-DC Interface

The AC-DC interface was modelled using the power balance over the converters to link the linear model of DC system and AC grid:

$$\begin{aligned} P_{dc} &= P_{ac} \\ Q_{dc} &= Q_{ac} \end{aligned} \quad (5\text{-}8)$$

5.1.2.1. VSC AC-DC Interface

Considering the differences between LCC and VSC, the model of the AC-DC interface of these two terminals is different. In the VSC side, the active and reactive power are fully decoupled and thus, can be manipulated independently in the AC side. But only the active power gets transferred to the DC link [28]:

$$P = \frac{3}{2}\left(i_{gd} v_{gd} + i_{gq} v_{gq}\right) \quad (5\text{-}9)$$

The related linearized incremental expression is as follows:

$$\Delta P = \frac{3}{2}\left(i_{gd0}\Delta v_{gd} + \Delta i_{gd} v_{gd0} + i_{gq0}\Delta v_{gq} + \Delta i_{gq} v_{gq0}\right) \quad (5\text{-}10)$$

As for the LCC terminal, instead of the power in AC grid, the DC side active power is being controlled. And the reactive power transferred into the AC grid is determined together by the active power and the power factor angle ψ_r of the LCC:

$$\begin{aligned} P_{ac} &= I_{dc} V_{dc} \\ Q_{ac} &= P_{ac} \tan(\psi_r) \end{aligned} \tag{5-11}$$

The related incremental values are given by:

$$\begin{aligned} \Delta P_{ac} &= I_{dc0} \Delta V_{dc} + \Delta I_{dc} V_{dc0} \\ \Delta Q_{ac} &= I_{dc0} \Delta V_{dc} \tan(\psi_0) + \Delta I_{dc} V_{dc0} \tan(\psi_0) + I_{dc0} V_{dc0} \frac{\Delta \psi}{\cos^2 \psi} \end{aligned} \tag{5-12}$$

With the active and reactive power, the AC grid current can be calculated in *q-d* frame as:

$$\begin{aligned} i_d &= \frac{3}{2} \frac{V_d P + V_q Q}{V_d{}^2 + V_q{}^2} \\ i_q &= \frac{3}{2} \frac{V_q P - V_d Q}{V_d{}^2 + V_q{}^2} \end{aligned} \tag{5-13}$$

DC side capacitor of VSC is included in the AC-DC interface. The VSC rectifier terminal is used as an example to explain the model of the AC-DC interface as shown in Figure 5.3. The VSC DC terminal voltage is determined by the current injected into and flows out of the capacitor:

$$\dot{V}_{dc} = \frac{I_r - I_{r1}}{C_{\text{vsc}}} \tag{5-14}$$

where the current I_r is decided by the active power exchange between the AC and DC grid. Also, I_{r1} can be calculated from the DC network dynamics.

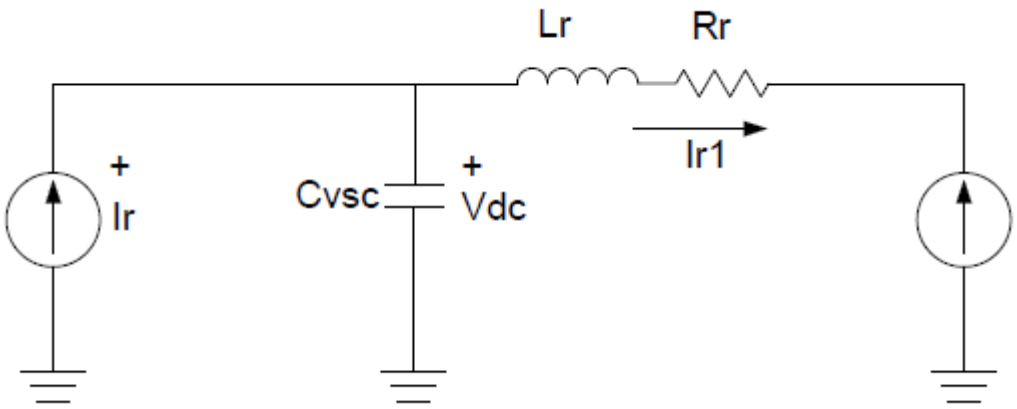

Figure 5.3 LCC AC grid equivalent circuit

5.1.3. LCC AC-DC Interface

Depends on the operation modes of rectifier or inverter, the LCC has the average output DC voltage as follows:

$$\begin{aligned} V_r &= \frac{3\sqrt{2}}{\pi} V_{LL,r} \cos(\alpha_r) - \frac{3\omega_r L_{ac,r}}{\pi} I_r \\ V_i &= -\frac{3\sqrt{2}}{\pi} V_{LL,i} \cos(\alpha_i) + \frac{3\omega_i L_{ac,i}}{\pi} I_i \end{aligned} \tag{5-15}$$

The related incremental expressions are:

$$\begin{aligned} \Delta V_r &= \frac{3\sqrt{2}}{\pi} \cos(\alpha_{r0}) \Delta V_{LL,r} - \frac{3\sqrt{2}}{\pi} V_{LL,r0} \sin(\alpha_{r0}) \Delta\alpha_r - \frac{3\omega_r L_{ac,r}}{\pi} \Delta I_r \\ \Delta V_i &= -\frac{3\sqrt{2}}{\pi} \cos(\alpha_{i0}) \Delta V_{LL,i} + \frac{3\sqrt{2}}{\pi} V_{LL,i0} \sin(\alpha_{i0}) \Delta\alpha_i + \frac{3\omega_i L_{ac,i}}{\pi} \Delta I_i \end{aligned} \tag{5-16}$$

5.1.4. DC Link

The DC link for the hybrid LCC-VSC connection is the same as the DC system modelled in the LCC-HVDC and VSC HVDC small-signal model, as shown in Figure 5.4. Note that in the following diagram, the inductor L_r and L_i include the inductance from the DC cable and the smoothing inductor from LCC DC terminal.

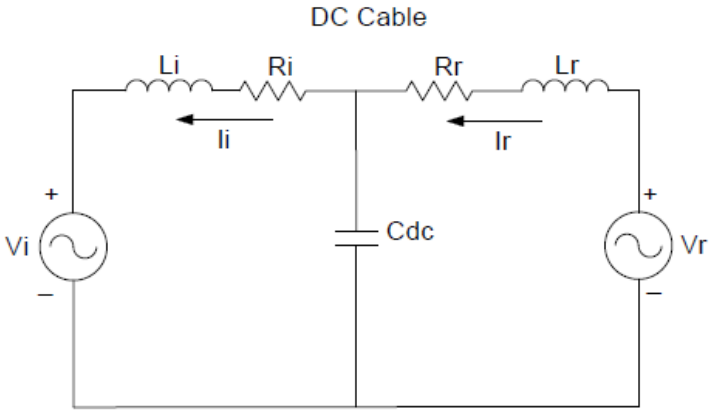

Figure 5.4 Equivalent circuit of DC link in hybrid HVDC connection

The DC system is modelled using the T-equivalent circuit as follows:

$$\begin{aligned} V_r &= I_r(R_r + sL_r) + V_{dc} \\ V_i &= -I_i(R_i + sL_i) + V_{dc} \\ sC_{dc}V_{dc} &= I_r - I_i \end{aligned} \tag{5-17}$$

Then, the state-space function of the DC network with two terminal connection is organized as:

$$\begin{bmatrix} \Delta\dot{I}_r \\ \Delta\dot{I}_i \\ \Delta\dot{V}_{dc} \end{bmatrix} = \begin{bmatrix} -\frac{R_r}{L_r} & 0 & -1 \\ 0 & -\frac{R_i}{L_i} & \frac{1}{L_i} \\ \frac{1}{C_{dc}} & -\frac{1}{C_{dc}} & 0 \end{bmatrix} \begin{bmatrix} \Delta I_r \\ \Delta I_i \\ \Delta V_{dc} \end{bmatrix} + \begin{bmatrix} \frac{1}{L_r} & 0 \\ 0 & -\frac{1}{L_i} \\ 0 & 0 \end{bmatrix} \begin{bmatrix} \Delta V_r \\ \Delta V_i \end{bmatrix} \tag{5-18}$$

5.1.5. PLL

The closed-loop function of the PLL tracking system can be linearized as [29]:

$$\Delta e_\theta = \frac{k_{p-pll}s + k_{i-pll}}{s^2 + k_{p-pll}v_q^0 s + k_{i-pll}v_q^0} \Delta v_d \tag{5-19}$$

where, e_θ is the angle deviation between grid voltage angle and the estimated angle from PLL and k_{p-pll} and k_{i-pll} are the proportional and integral gain of the controller. The deviation between the grid and the estimated angular position can be integrated into the model through

the rotation of angle deviation. Then, the synchronous reference frame variables based on the grid angle and the frame based on the PLL estimated angle can be linked using the following transformation:

$$\begin{bmatrix} \Delta X_d \\ \Delta X_q \end{bmatrix} = \mathrm{T}_{dq} \begin{bmatrix} \Delta X_{dc} \\ \Delta X_{qc} \end{bmatrix} \tag{5-20}$$

where, the transformation matrix is:

$$T_{dq} = \begin{bmatrix} \cos(e_{\theta_0}) & -\sin(e_{\theta_0}) & -\sin(e_{\theta_0})x_{q_0} - \cos(e_{\theta_0})x_{d_0} \\ \sin(e_{\theta_0}) & \cos(e_{\theta_0}) & \cos(e_{\theta_0})x_{q_0} - \sin(e_{\theta_0})x_{d_0} \end{bmatrix} \tag{5-21}$$

Also, its inverse transformation ca be defined as:

$$\begin{bmatrix} \Delta X_{dc} \\ \Delta X_{qc} \end{bmatrix} = \mathrm{T}_{dc}^{-1} \begin{bmatrix} \Delta X_d \\ \Delta X_q \end{bmatrix} \tag{5-22}$$

where the inverse transformation matrix is:

$$T_{dq}^{-1} = \begin{bmatrix} \cos(e_{\theta_0}) & \sin(e_{\theta_0}) & \cos(e_{\theta_0})x_{d_0} - \sin(e_{\theta_0})x_{q_0} \\ -\sin(e_{\theta_0}) & \cos(e_{\theta_0}) & -\cos(e_{\theta_0})x_{q_0} - \sin(e_{\theta_0})x_{d_0} \end{bmatrix} \tag{5-23}$$

5.1.6. Small-signal Complete Model

With the linear model developed in the previous section, each subsystem of the hybrid LCC-HVDC connection has been studied. Figure 5.5 shows the complete structure of the small-signal model:

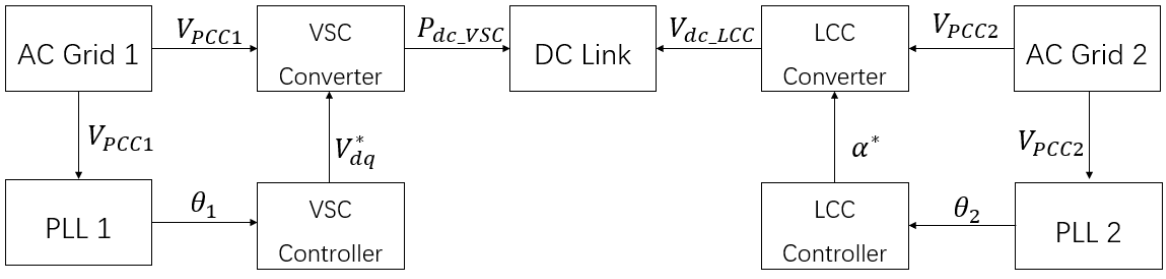

Figure 5.5 Small-signal complete model of hybrid HVDC system

5.2. Validation of Hybrid Linear Model

In the small-signal model, the linearized point was selected to be the nominal operating point of the HVDC transmission system. In this section, the simulation results among four hybrid connection configurations, generated from the small-signal model, the average model and the detailed nonlinear model including switching dynamics, were plotted respectively from Figure 5.6 to Figure 5.13. The accuracy of the small-signal models was verified by comparing the simulation results. The performance of the designed control system was tested by driving the voltage or current to track the step variation of their reference.

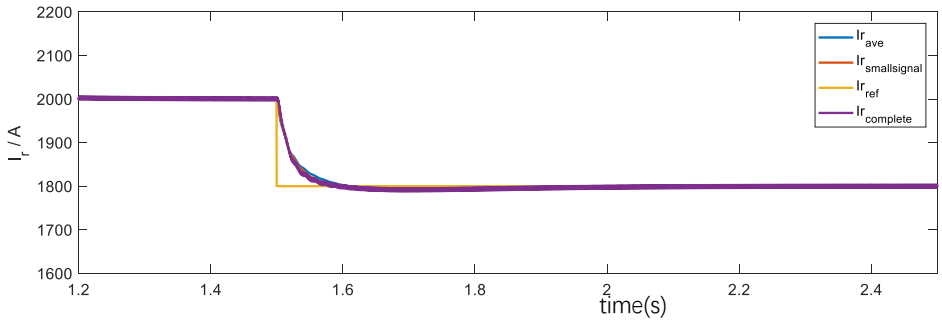

Figure 5.6 Rectifier DC current of hybrid configuration 1

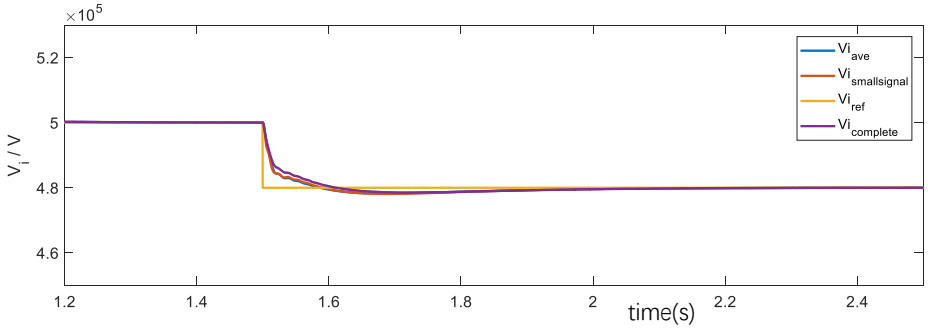

Figure 5.7 Inverter DC terminal voltage of hybrid configuration 1

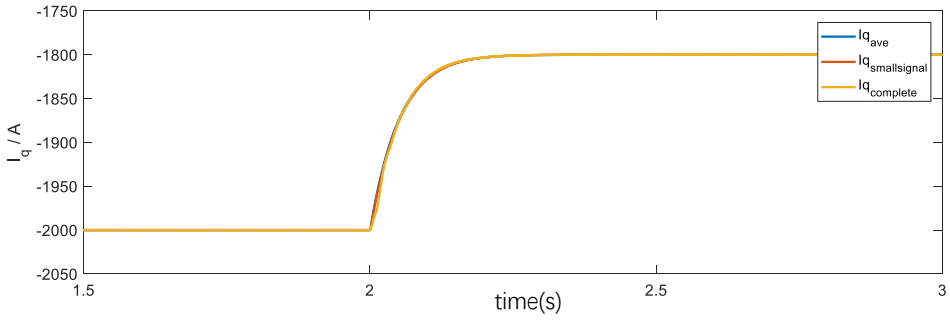

Figure 5.8 Inverter AC terminal current (q-axis component) of hybrid configuration 2

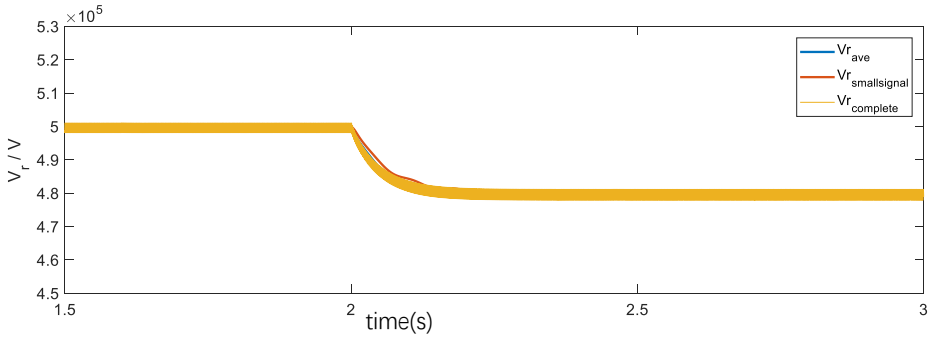

Figure 5.9 Rectifier DC terminal voltage of hybrid configuration 2

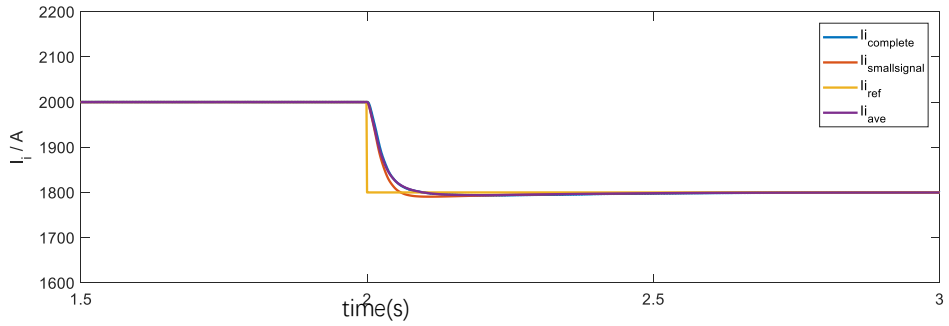

Figure 5.10 Inverter DC terminal current of hybrid configuration 3

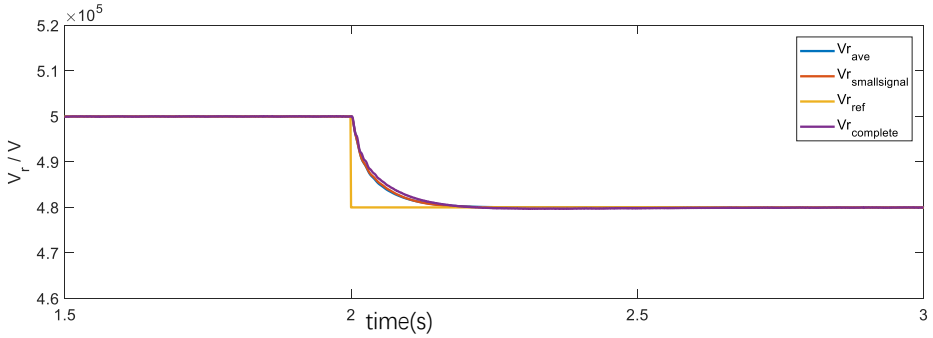

Figure 5.11 Rectifier DC terminal voltage of hybrid configuration 3

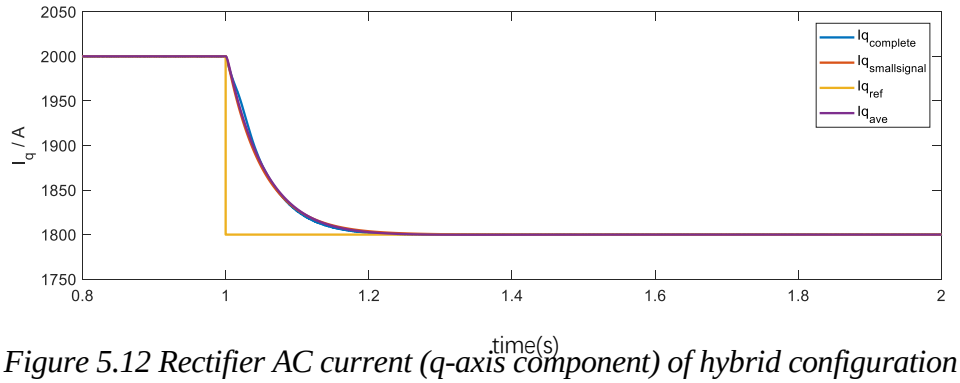

Figure 5.12 Rectifier AC current (q-axis component) of hybrid configuration 4

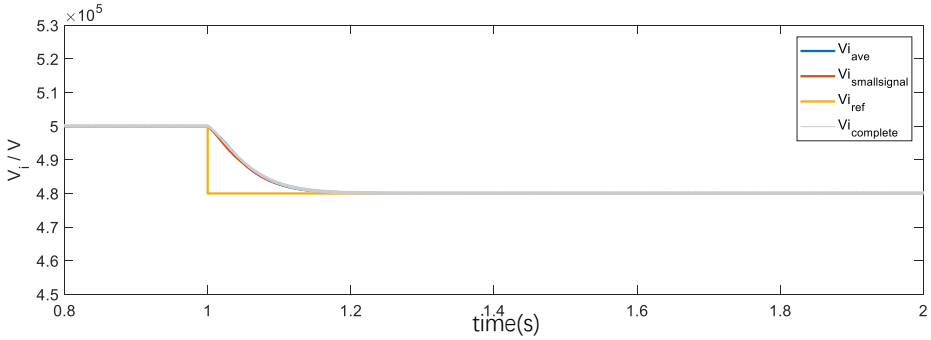

Figure 5.13 Inverter DC terminal voltage of hybrid configuration 4

5.3. Small-signal Model Analysis of Hybrid HVDC System

In this section, the eigenvalue analysis has been conducted based on the complete linear model for each hybrid HVDC configuration. The natural frequency and damping corresponding to each pole in the linear model are listed in Appendix C. Eigen Value of Hybrid HVDC System Small-Signal Model. Also, the normalized participation factors to each mode coming from different state variables have been calculated based on the state-space matrix of the complete linear model.

5.3.1. Analysis of Hybrid HVDC Configuration 1: LCC$_v$-VSC$_i$

As it can be seen in the participation factor results in Table C.2. two pairs of undamped poles with frequency of 220.46 Hz and 206.45 Hz are related to the AC dynamics of the grid connected at the LCC rectifier terminal. Mode 6 at 363.85 Hz is participated by the VSC inverter AC grid dynamics and Mode 8 to 11 with frequency varied from 75.61 Hz to 17.55 Hz are influenced by the DC variables at both rectifier and inverter terminal, which indicates the interaction between the operation of LCC and VSC in this hybrid HVDC connection.

Besides, the high-damped mode 7 with natural frequency at 98.31Hz is highly participated by the error in estimated angular position from PLL in the LCC rectifier connected AC grid, while mode 16 and 17 of 149.54 Hz are corresponding to the PLL at VSC inverter side AC grid.

5.3.2. Analysis of Hybrid HVDC Configuration 2: LCC_i-VSC_v

In configuration 2, the participation factor results in Table C.4 shows a mode at 1023.44 Hz corresponding to the DC terminal current regulated by LCC rectifier. Besides, two pairs of poles in mode 2, 3 at 346.94 Hz and mode 10, 11 at 222.84 Hz are participated by both VSC inverter side AC dynamics and DC variables. Thus, these four modes reveal the AC-DC interaction for the VSC terminal in configuration 2. Mode 5 to 8 with frequency between 220.79 to 207.96 Hz are four undamped modes participated only by the LCC rectifier side AC grid dynamics.

Mode 17 and 18 are related to a pair of low frequency poles at 3.97 Hz are participated by both the reference value integral of rectifier DC terminal current and the integral value of q-axis current component at LCC inverter side AC grid. Thus, modes 17 and 18 show a high correlation between both converters in the operation of configuration 2. Additionally, pole 9 and pole 15 are corresponding to the mode of PLL at rectifier side and inverter side respectively.

5.3.3. Analysis of Hybrid HVDC Configuration 3: VSC_v-LCC_i

In configuration 3, the participation factors, as listed in Table C.6, have a mode with natural frequency at 2611.71 Hz is highly participated by the LCC inverter terminal DC current. While mode 2 at 282.54 Hz and mode 6 to 10 with frequency slightly higher than 200 Hz are related to AC grid dynamics at the LCC inverter side. Additionally, two pairs of pole in modes 4-5 and 10-11 are participated jointly by V_{dci} and AC and DC dynamics at VSC rectifier side. Thus, these four modes, with natural frequencies at 253.87 and 60.43 Hz show an interaction between rectifier and inverter terminals. This kind of interaction of the LCC inverter will be expressed as the fluctuation of V_{dci}.

Another mode worth mention is mode 12. This low frequency high-damped mode is participated by the rectifier side AC dynamics including the angular error coming from PLL and inverter side DC voltage. This mode indicates that the PLL dynamics will not only affect the AC dynamics but are also coupled with the DC link variable.

5.3.4. Analysis of Hybrid HVDC Configuration 4: VSC_i-LCC_v

The first four modes of configuration 4 are only participated by inverter AC grid components (see Table C.8) with the frequency at 222.19 and 209.58 Hz. Thus, they can be defined as the

mode related to AC dynamics of the grid connected with LCC inverter. The other two pairs of modes 6-7 and 9-10 with frequency of 75.20 and 18.68 Hz respectively, are jointly participated by DC variables at both rectifier and inverter terminal. Thus, according to these low frequency modes a high correlation between the operation of LCC and VSC can be verified. Furthermore, mode 5 with natural frequency of 97.45 Hz is related to LCC inverter side PLL while mode 12-13 at 179.85 Hz is dominated by VSC rectifier side PLL and AC grid elements.

5.4. Hybrid Small-signal Model Parameters Sensitivity Analysis

With the small-signal model constructed respectively for four hybrid HVDC configurations, the pole analysis is conducted to investigate the system stability and dynamics in response to the variation of system parameters including DC cable length and AC grid strength as well as the converters controller speed. The dominant poles to each mode revealed from section 5.3 are mapped to demonstrate the influence of different parameters to the system stability. Also, result from the detailed non-linear model were also plotted for hybrid configuration 2 in order to verify our analysis of small-signal models.

5.4.1. DC Cable Length

The poles map in response to the DC cable length increase is plotted in Figure 5.14. The result shows that in the two configurations where LCC were adopted as the rectifier, the extension of DC cable can lead to the instability of the transmission system. While for the other two hybrid configurations in which the VSC is working as the rectifier, the system stability margin will be reduced with the increase of DC cable length. Note that increase the DC cable length during the operation of the an transmission system is unrealistic. Thus, the simulation result if not showed in this subsection. The dominant poles in response to the DC cable length are related to the DC dynamics or interaction of both converters in DC link.

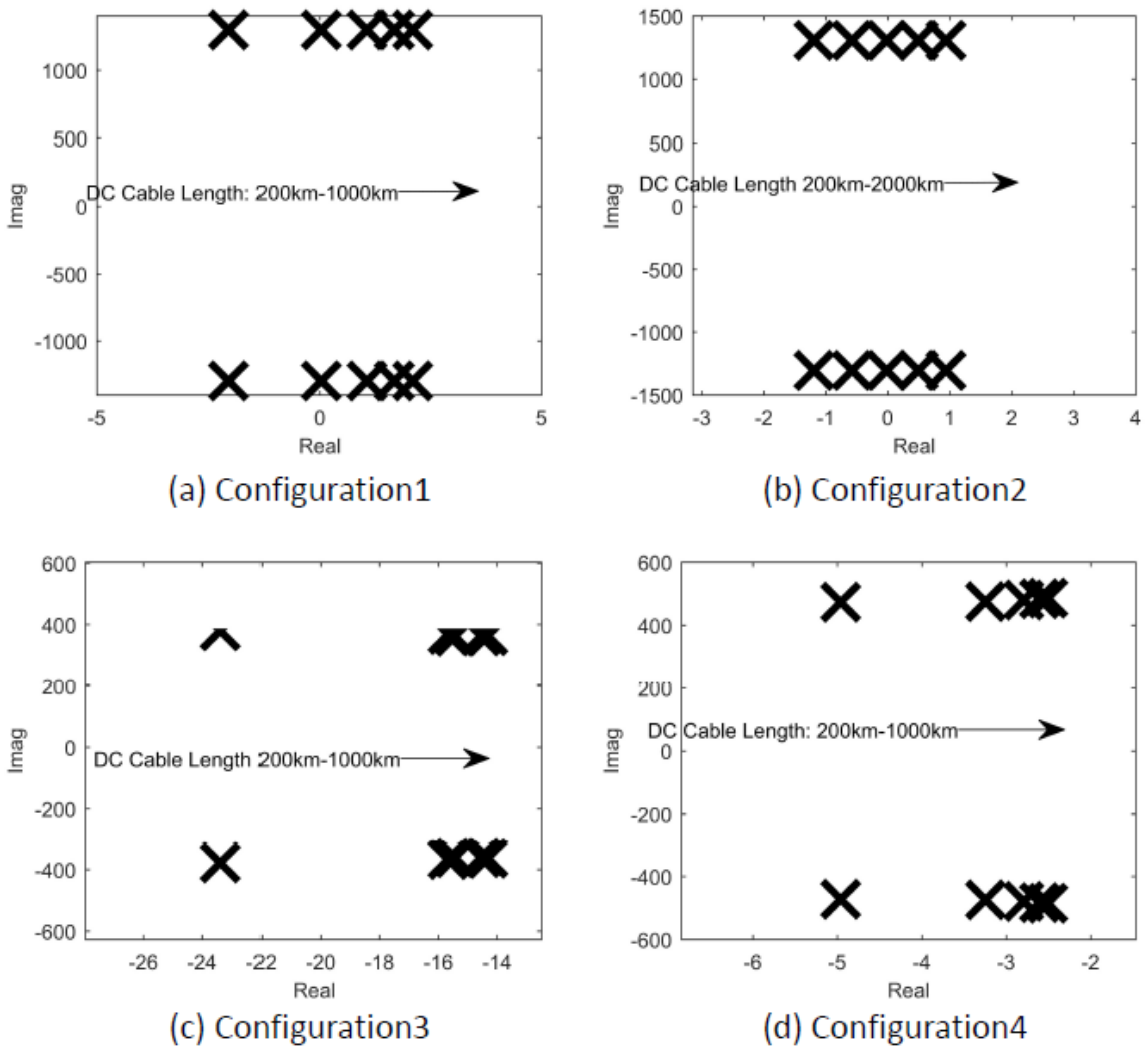

Figure 5.14 Poles map-DC cable length

5.4.2. LCC Voltage Controller Speed

The proportional and integral gains of the LCC voltage has been decreased by up to 10 times here to test the HVDC system sensitivity to the controller speed. The poles movement in Figure 5.15 indicates that with the decrease of both K_p and K_i in LCC voltage controller, the system stability margin will be reduced for both configuration 1 and configuration 4. However, instability cannot be observed with the voltage controller parameter variation. Dominant poles are from the mode with high participation factor from DC voltage. In particular, for configuration 1, the dominant poles are related to the AC-DC interaction mode. However, the dominant poles in configuration 4 are related to the DC link dynamics mode.

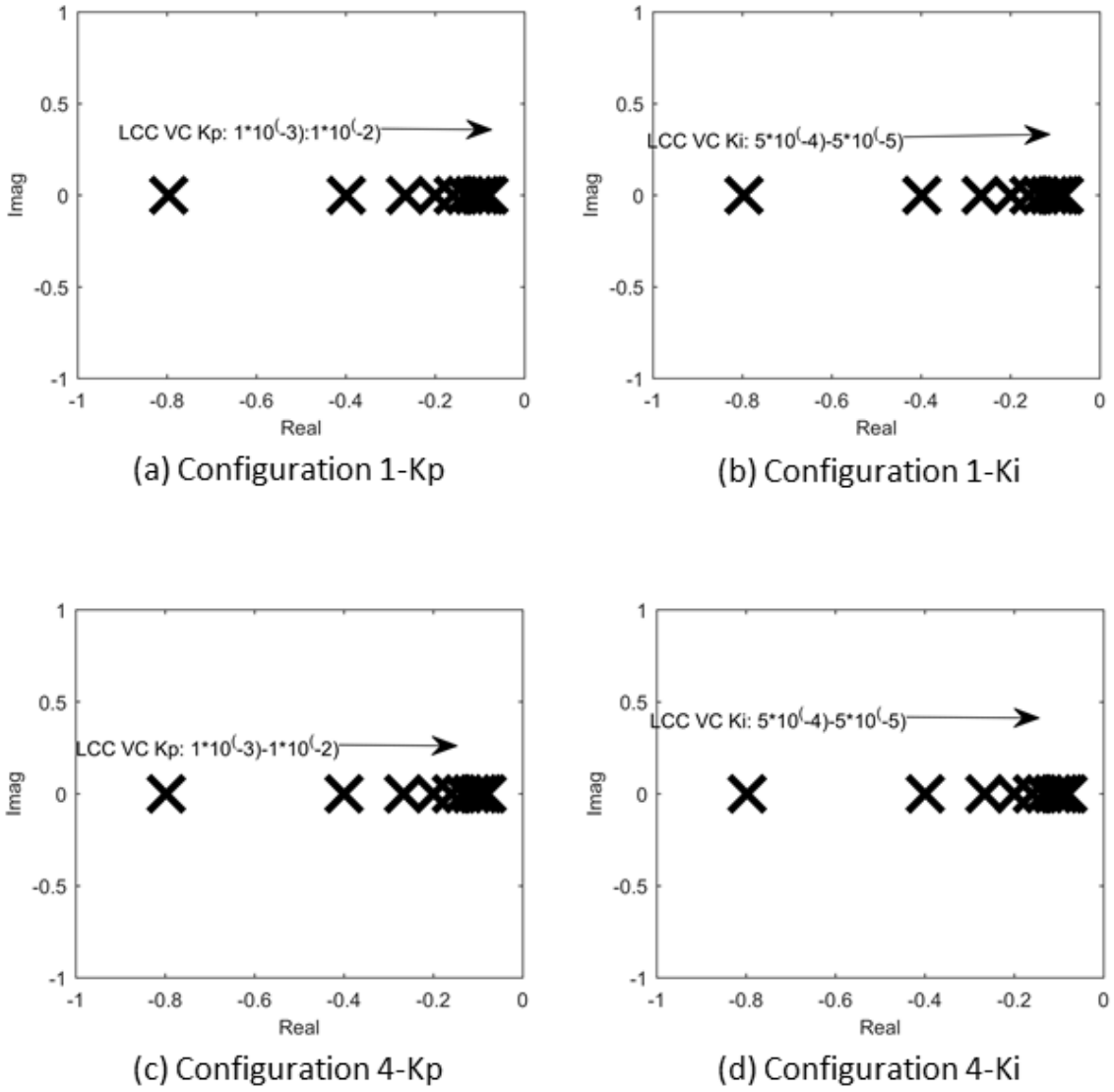

Figure 5.15 Poles map-LCC voltage controller

5.4.3. LCC Current Controller Speed

The LCC current controller speed has been tested in this section by increasing the controller gain K_p and K_i up to 10 times respectively. The results from the linear model (see Figure 5.16) show that with the increase of LCC current control speed, the system stability margin will be reduced. However, the increased speed of LCC current controller will not result in instability of the transmission system. The dominant poles that are sensitive to the LCC current controller are all related to LCC side AC dynamics.

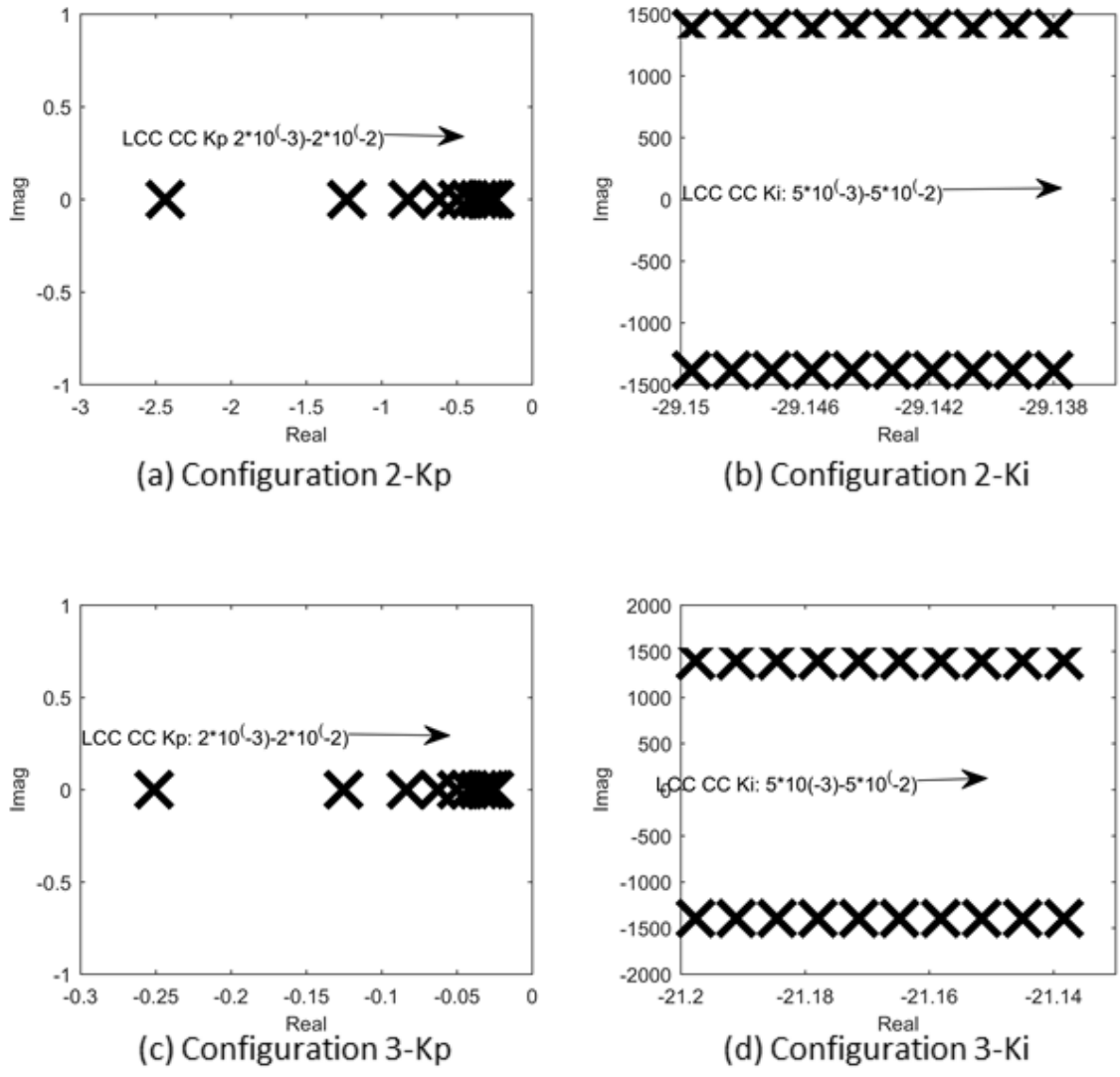

Figure 5.16 Poles map-LCC current controller

The time domain simulation from configuration 2 non-linear model is showed in Figure 5.17, Figure 5.18 below to verify the result. With the increased the LCC current speed, the DC current is still stable but higher overshoot and oscillation magnitute can be found from the current dynamics.

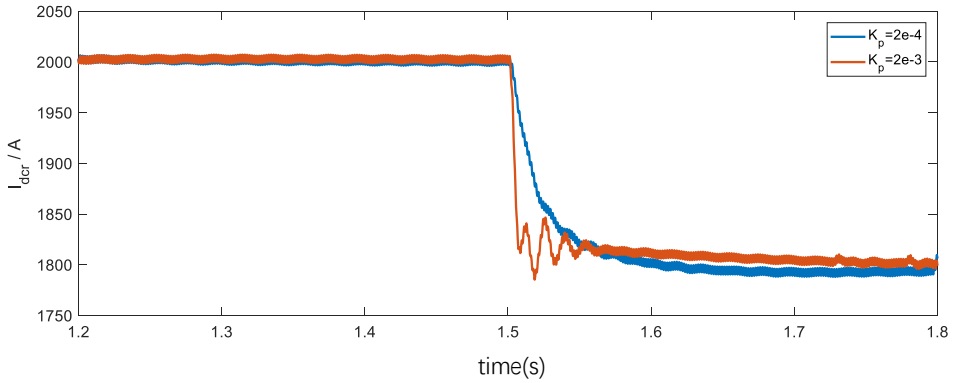

Figure 5.17 Rectifier DC terminal current-LCC current controller Kp configuration 2

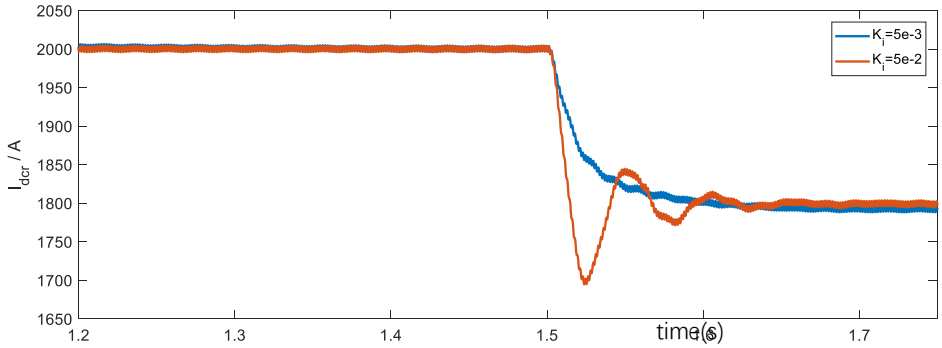

Figure 5.18 Rectifier DC terminal current-LCC current controller Ki configuration 2

5.4.4. VSC Voltage Controller Speed

The VSC voltage controller in configurations 2-3 showed a dramatical influence to the system stability since, in these two configurations, the decrease of the voltage controller's proportional gain may create instability to the system (see poles maps in Figure 5.19). Dominant poles being sensitive to the VSC DC voltage controller are corresponding to the mode of VSC side AC dynamics or AC-DC interaction of VSC.

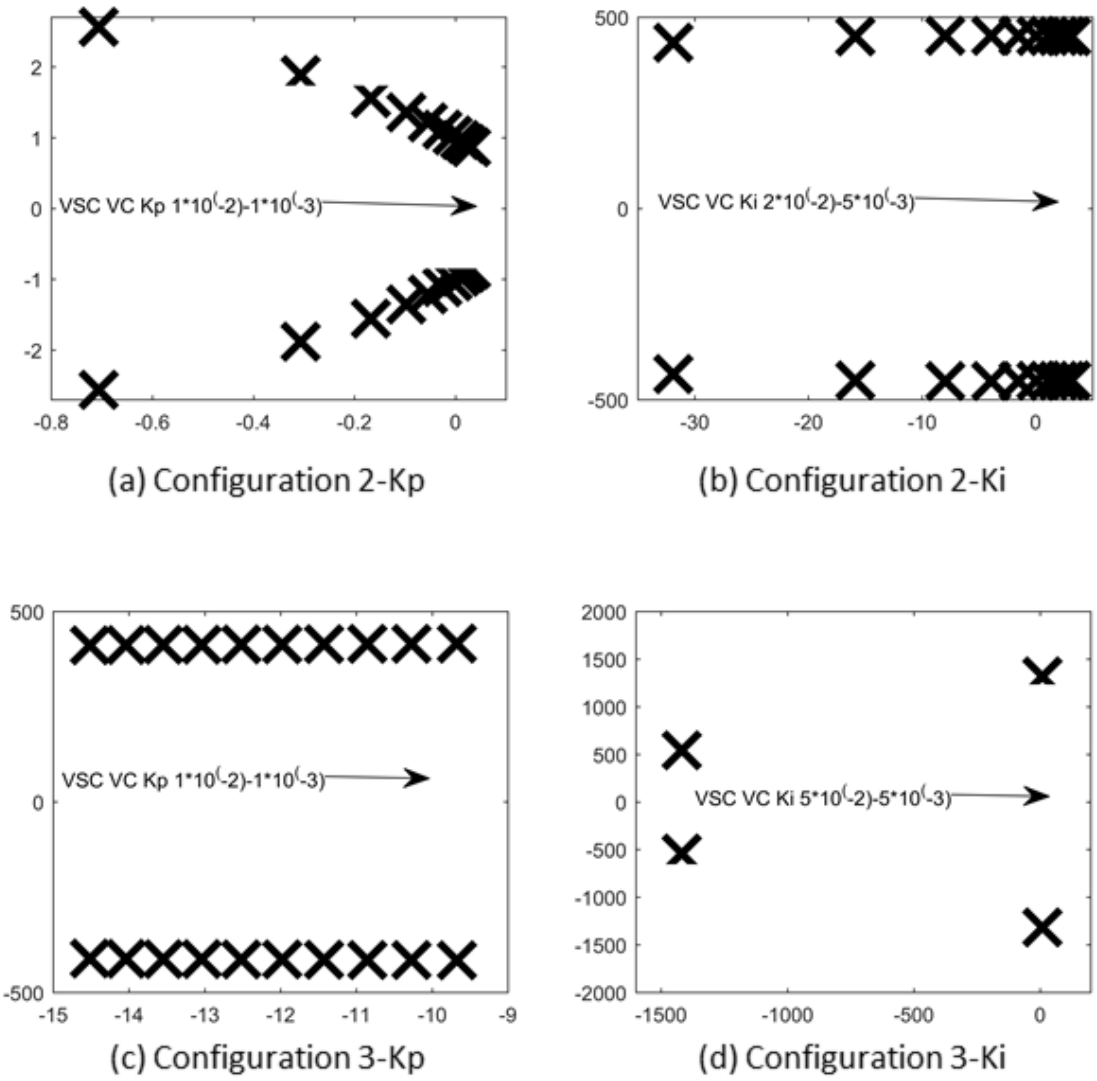

Figure 5.19 Poles map-VSC voltage controller

Figure 5.20 and Figure 5.21 show the time-domain simulation of configuration 2 corresponding to different VSC voltage controller parameters.

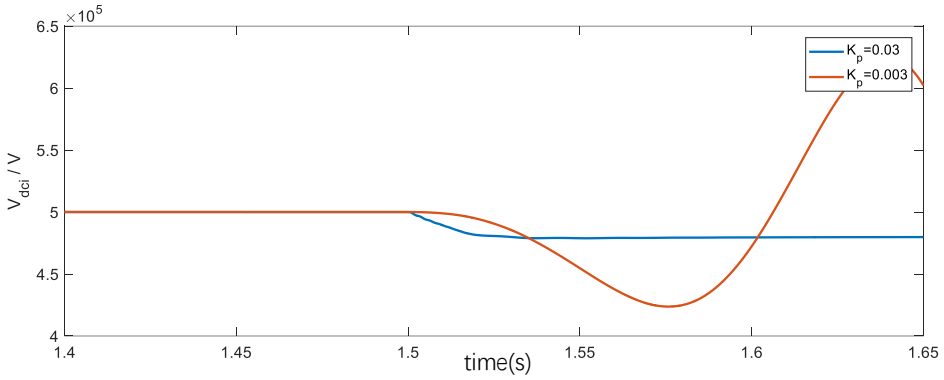

Figure 5.20 Inverter DC terminal voltage-inverter voltage controller Kp configuration 2

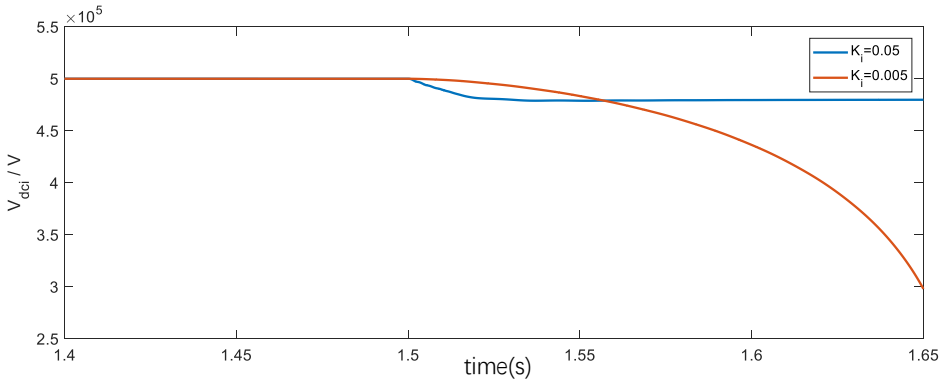

Figure 5.21 Inverter DC terminal voltage-inverter voltage controller Ki configuration 2

5.4.5. VSC Current Controller Speed

The speed of the VSC current controller is dominated by the time constant τ. The linear model of hybrid configuration 1 and 4 indicates that when the VSC is working at the control mode of AC current, the decrease of its current controller speed will reduce the stability margin but will not affect the system stability. The poles maps are shown in Figure 5.22. The dominant poles being analyzed in this subsection belong to the modes of DC interaction between the converters.

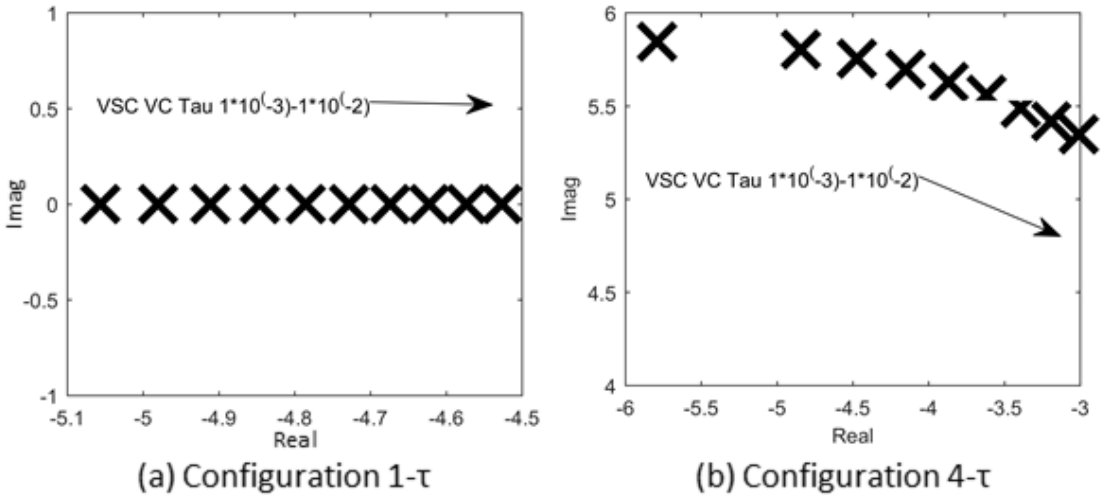

Figure 5.22 Poles map-VSC current controller

5.4.6. AC Grid Strength

The strength of the AC grid is defined by its short circuit ratio (SCR) [30]:

$$SCR = \frac{S_{sc}}{P_N} \tag{5-24}$$

where S_{sc} stands for the short circuit capacity of the AC grid and P_N is the nominal power.

When the SCR of the AC grids is reduced, all of four configurations show similar response. Independently of the LCC or VSC side, the system will become unstable (see Figure 5.23). Also, the VSC has higher capacity to be connected to weak grid compared to LCC terminal among all of four hybrid configurations (see Figure 5.24). The dominant poles of AC grid SCR variation are from the mode of AC dynamics.

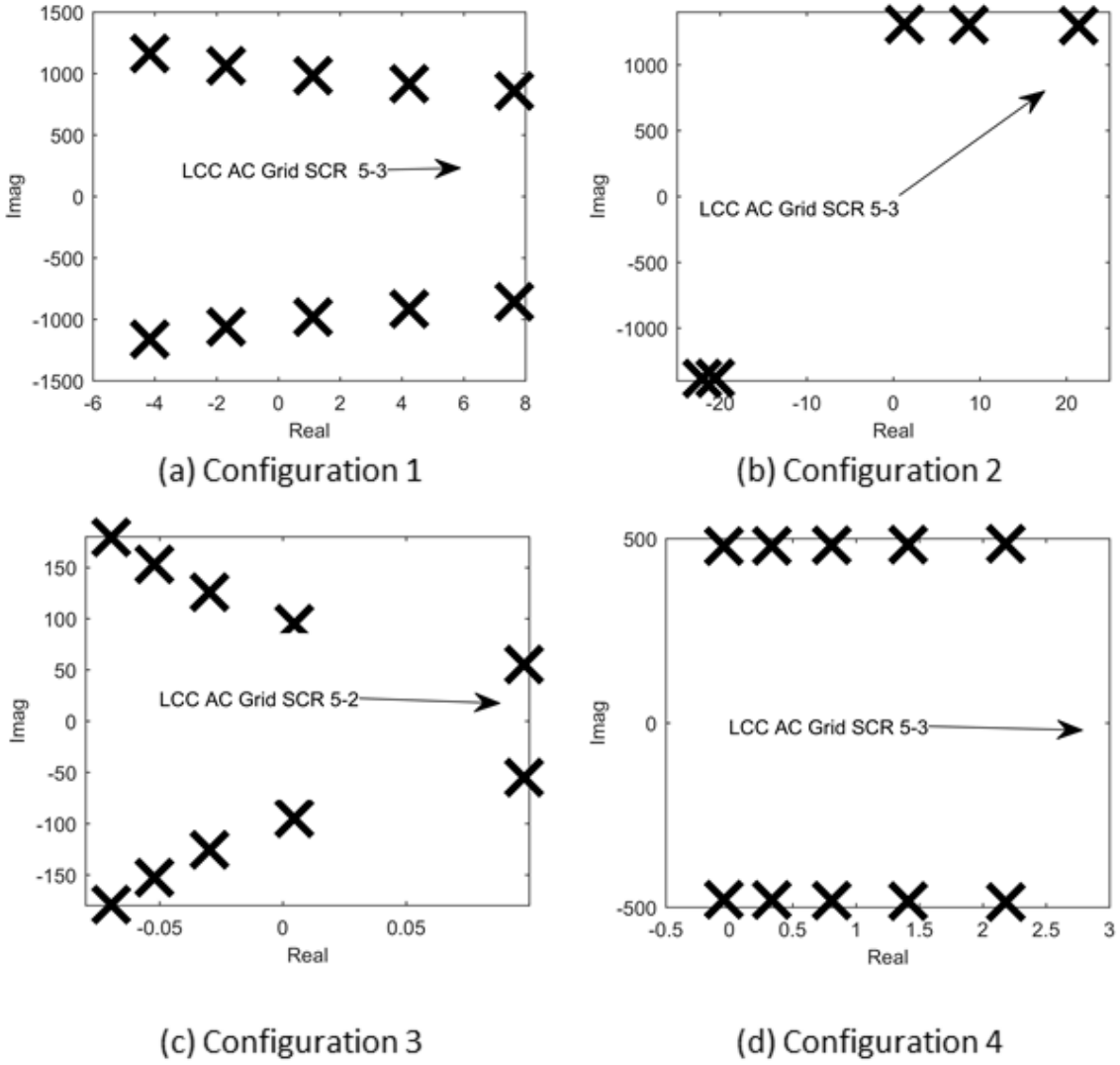

Figure 5.23 Poles map-LCC AC grid SCR

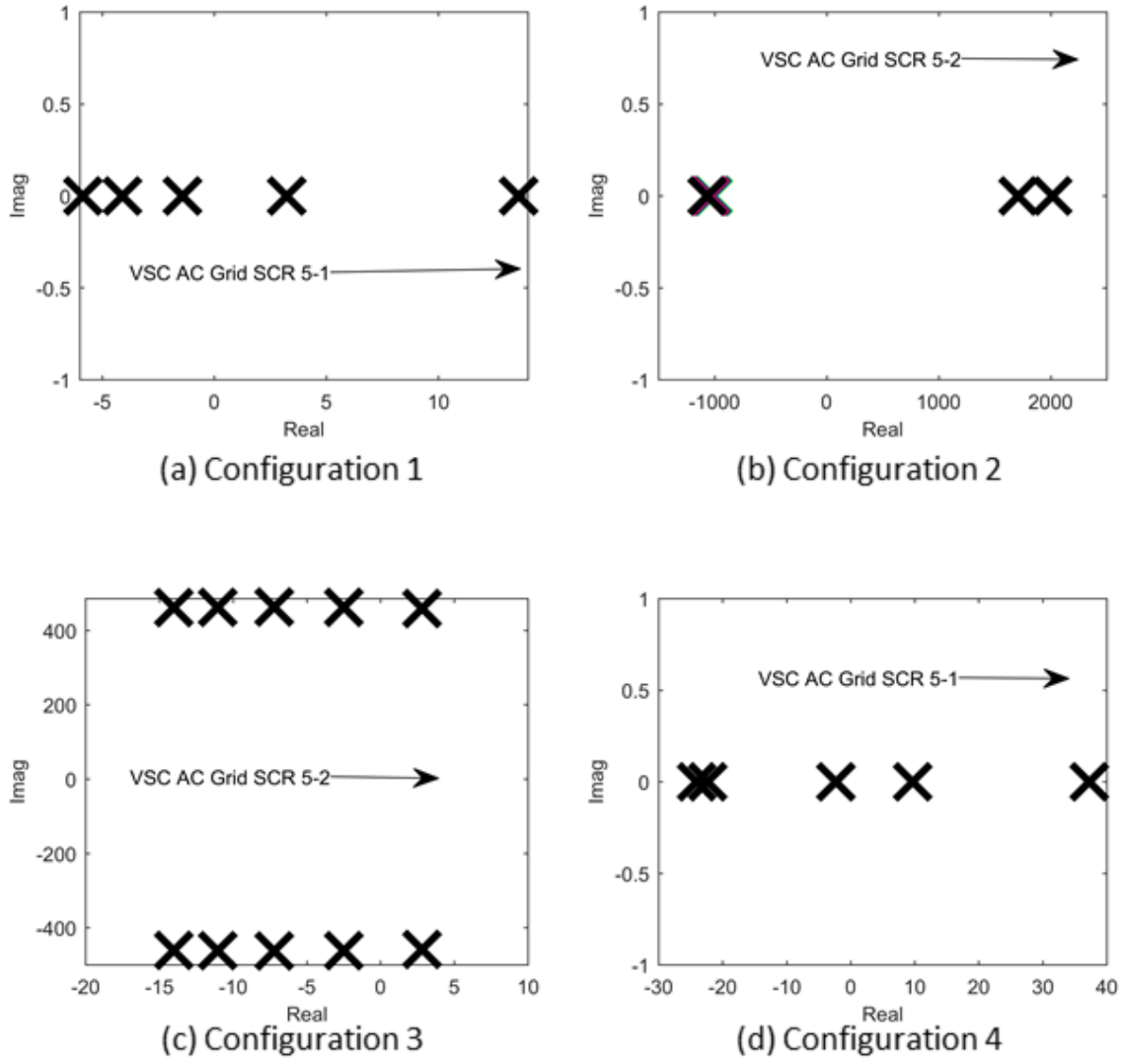

Figure 5.24 Poles map-VSC AC grid SCR

With the reduced AC grid SCR, the instability can also be observed from the time-domain simulation result of configuration 2 in Figure 5.25:

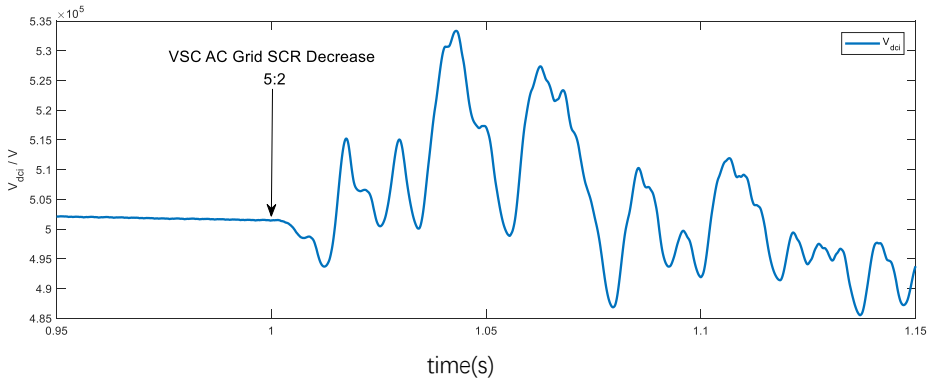

Figure 5.25 Inverter DC terminal voltage-reduced VSC AC grid SCR configuration 2

5.4.7. PLL

The influence of PLL controller's speed to the system stability has been tested on each of hybrid configuration respectively. The result shows that when increasing the PLL speed by multiplying its proportional and integral gains in the controller by up to10 times. In either VSC or LCC side AC grid, the system stability margin will be reduced. However, the instability will not be caused by PLL. Dominant poles related to PLL are from AC grid dynamics or AC-DC interactions.

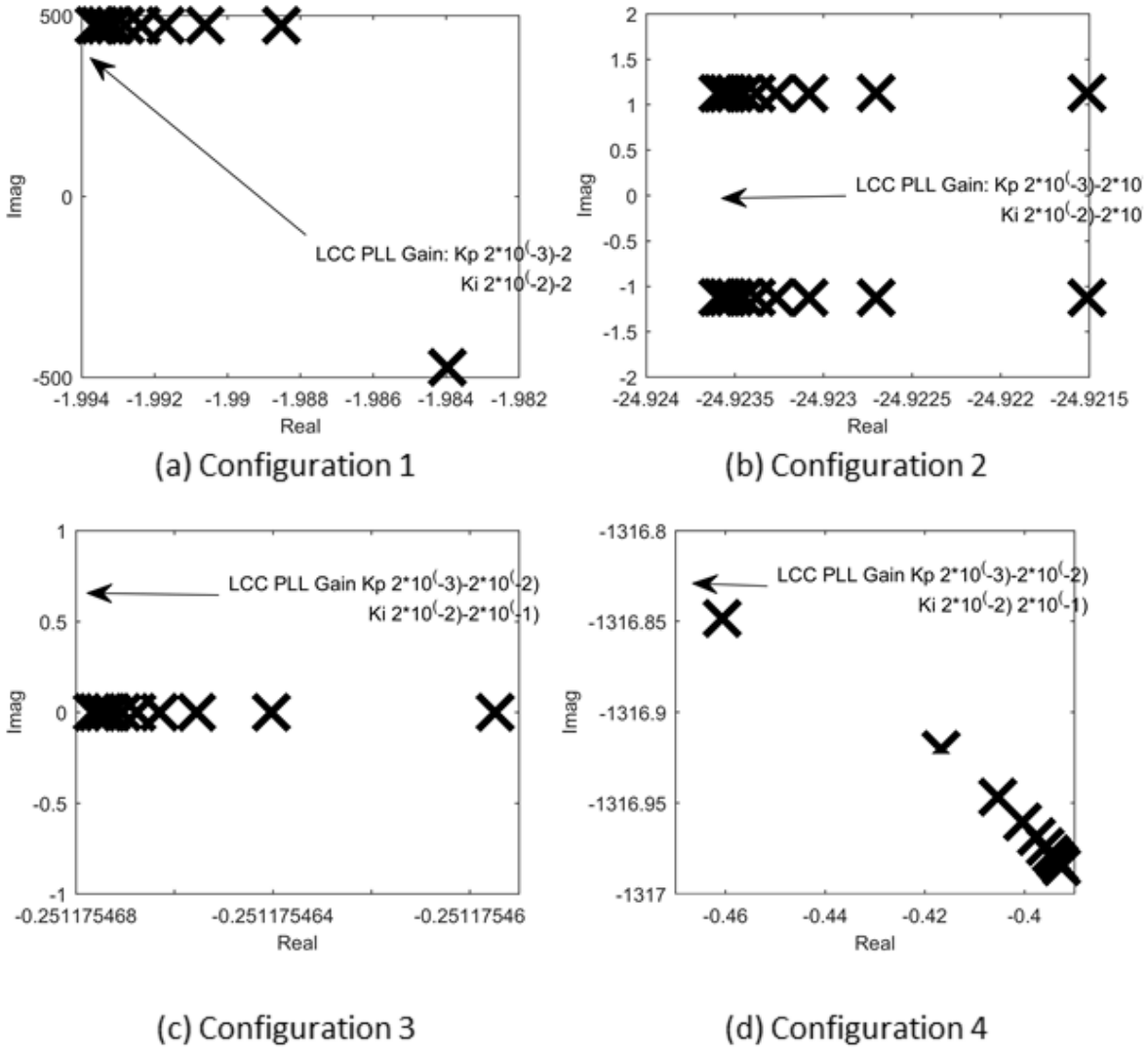

Figure 5.26 Poles map-LCC AC grid PLL

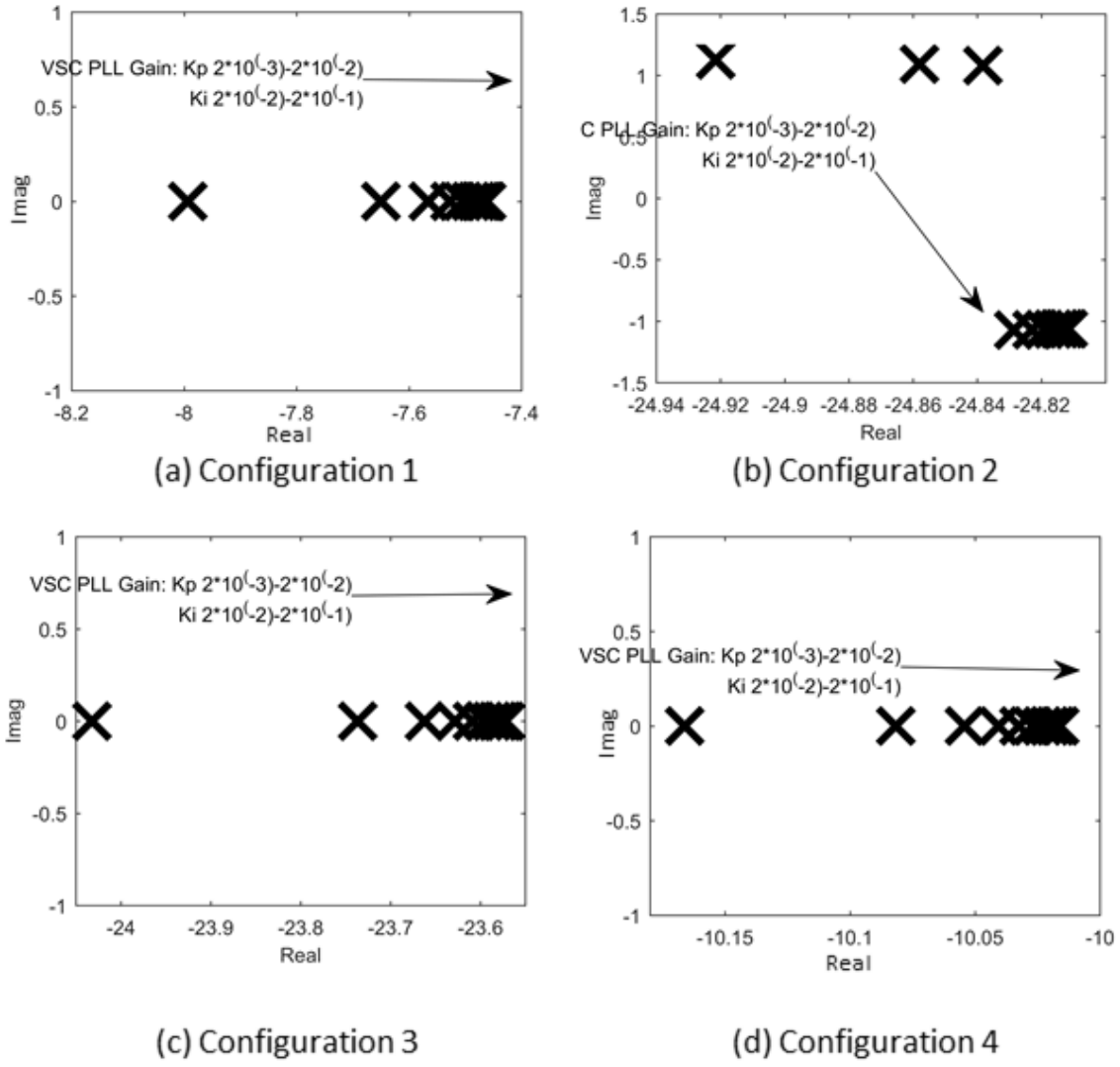

Figure 5.27 Poles map-VSC AC grid PLL

Also, the simulation result from configuration 2 was plotted to show the dynamics influenced by the PLL speed. Scenarios with K_p and K_i gains with originally designed value and up to 10 times higher the initial value are being tested in this subsection. In Figure 5.28, higher oscillation can be found in the LCC terminal DC current with the increased speed of LCC side PLL speed. Also, the DC voltage control at the VSC side shows the same trend in Figure 5.29 that when the VSC connected PLL is faster, the higher oscillation can be found on the DC voltage waveforms.

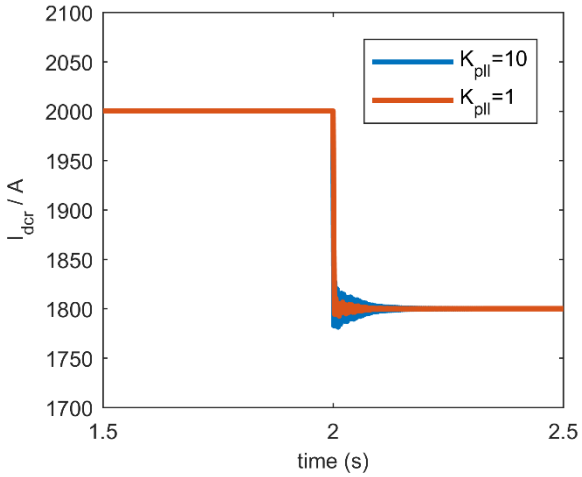

Figure 5.28 Rectifier DC current-LCC PLL configuration 2

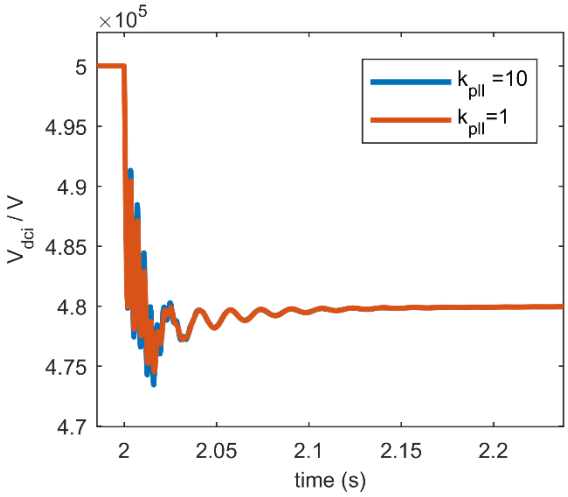

Figure 5.29 Inverter DC voltage-VSC PLL configuration 2

6. Conclusion

6.1. Contributions

This thesis presented the modelling and analysis of the hybrid VSC-LCC HVDC transmission system as well as the design of its operational and controlling strategy. The contributions in this thesis are listed as follows:

1. The working principle of LCC-HVDC and VSC-HVDC has been understood.

2. An analytical model has been constructed for LCC-HVDC and VSC-HVDC respectively using MATLAB/Simulink. Also, the control scheme for LCC-HVC and VSC-HVDC has been explained and tested in this thesis.

3. Four different configurations of hybrid LCC-VSC HVDC transmission system has been compared and analyzed. The operation strategies have been proposed for different configurations.

4. Small-signal model has been constructed for different configurations of hybrid LCC-VSC HVDC. The small-signal model accuracy has been verified by comparing the simulation results from non-linear models.

5. Analysis of hybrid VSC-LCC HVDC system has been conducted based on its small-signal model. The influence to the system dynamics of different components, including the DC cable length, AC grid strength and the parameters of the converter controllers has been studied.

6.2. Comparison of Hybrid HVDC Configurations

From the modeling, simulation and linear model based analysis in the previous sections of the hybrid LCC-VSC HVDC system, the system characteristics have been studied. In summary, the operation of both rectifier and inverter are interacted with each other in the point-to-point hybrid connection. Also, the AC grids and DC link is highly correlated in both converter terminals. However, different hybrid HVDC configurations have different dynamics and operational features. And the comparison of these four configurations can be seen in Table 6.1.

Table 6.1 Comparision of hybrid VSC-LCC HVDC configurations

Configurations	Advantage	Disadvantage	Application Scenario
$LCC_v - VSC_i$	-Fast current dynamics -Precharged by both converters -Capability feeding weak grid	Limitation on DC cable length	Feed to weak or passive grid
$LCC_i - VSC_v$	-Fast DC voltage dynamics -Precharged by both converters -Capability feeding weak grid	Limitation on DC cable length	Feed to weak or passive grid
$VSC_v - LCC_i$	-Fast DC voltage dynamics -Sending end AC grid support	LCC commutation failure risk	Integrate rewable generation
$VSC_i - LCC_v$	-Fast current dynamics -Sending end AC grid support	LCC commutation failure risk	Integrate rewable generation

The selection on hybrid configurations should consider the requirements of different application scenarios. However, configuration 2 $VSC_v - LCC_i$ is considered the best in general since it has highest stability margin.

6.3. Future Work

At the future work, the following tasks can be considered to carry out based on this thesis :

1. The small-signal model of the hybrid LCC-VSC HVDC system can be expanded with more AC grid dynamics including the AC filters and AC voltage frequency variation.

2. The fault ride through capability and strategy of the hybrid system can be studied.

3. The model can be expanded into multi-terminal HCDC system combining LCCs and VSCs to implement the interconnection of multiple grids.

Appendix A. Park Transformation

The Park transformation matrix can be written as:

$$T = \frac{2}{3}\begin{bmatrix} \cos(\theta) & \cos(\theta-\frac{2\pi}{3}) & \cos(\theta+\frac{2\pi}{3}) \\ \sin(\theta) & \sin(\theta-\frac{2\pi}{3}) & \sin(\theta+\frac{2\pi}{3}) \\ \frac{1}{2} & \frac{1}{2} & \frac{1}{2} \end{bmatrix} \quad \text{(A-1)}$$

and its inverse transformation matrix:

$$T^{-1} = \begin{bmatrix} \cos(\theta) & \sin(\theta) & 1 \\ \cos(\theta-\frac{2\pi}{3}) & \sin(\theta-\frac{2\pi}{3}) & 1 \\ \cos(\theta+\frac{2\pi}{3}) & \sin(\theta+\frac{2\pi}{3}) & 1 \end{bmatrix} \quad \text{(A-2)}$$

Appendix B. Environmental Impact of HVDC Transmission System

The result and achievement of the result are considered to promote the wider application of HVDC transmission technology. Thus, the environmental impact of the HVDC transmission system will be analyzed here can considered as an environmental impact of the thesis. The environmental impact of the HVDC transmission system can be categorized in the following aspects:

Impact of Transmission Line

Compared to the three-phase transmission line used in the HVAC system, the overhead line for HVDC transmission system is more compact. Thus, the environmental impact is reduced by minimizing the space occupation and the visual impact from the transmission line and electric towers [31]. Besides, due to the characteristic of direct current transmission, the intensity of electromagnetic interference generated from the transmission line is lower compared to AC transmission. Also, in some applications, the underground cable was considered as an alternatively solution, which can reduce the environmental impact further.

Lower Power Losses

In most of cases, the power losses of HVDC system is lower than the HVAC system with similar capacity. And with the energy saving among the transmission system, the significant amount of CO_2 emissions can be reduced yearly [32].

Integration of Renewable Energy

The HVDC has been proven have the advantages in integration of renewable energy source into the electric power grid. Especially the VSC based HVDC is considered to be one of the ideal technology for the application in the renewables generation side due to its compact size and flexible operation.

Appendix C. Eigen Value of Hybrid HVDC System Small-Signal Model

Table C.1 Natural frequency and damping of hybrid configuration 1 small signal model poles

Frequency(Hz)	Damping
220.46	0.02
220.46	0.02
153.50	1.00
206.45	0.01
206.45	0.01
363.85	1.00
98.31	1.00
75.61	0.01
75.61	0.01
17.55	0.10
17.55	0.10
5.13	1.00
2.83	1.00
1.61	1.00
3.41	1.00
149.54	0.75
149.54	0.75
1.47	1.00
1.27	1.00

Table C.2 Partifipation factors of hybrid configuration 1

Mode	1	2	3	4	5	6	7
Damping	0.02	0.02	1.00	0.01	0.01	1.00	1.00
Frequency(Hz)	220.46	220.46	153.50	206.45	206.45	363.85	98.31
I_dcr	0.00	0.00	0.06	0.01	0.01	0.00	0.12
I_dci	0.00	0.00	0.00	0.00	0.00	0.00	0.00
V_dc	0.00	0.00	0.00	0.00	0.00	0.00	0.01
V_dci	0.00	0.00	0.00	0.00	0.00	0.00	0.00
I_i_d	0.00	0.00	0.00	0.00	0.00	1.00	0.00
I_i_q	0.00	0.00	0.00	0.00	0.00	0.56	0.00
int V_dcr	0.00	0.00	0.00	0.00	0.00	0.00	0.00
int I_i_d (ms)	0.00	0.00	0.00	0.00	0.00	0.01	0.00
int I_i_q (ms)	0.00	0.00	0.00	0.00	0.00	0.00	0.00
I_r_q	1.00	1.00	0.00	0.17	0.17	0.00	0.00
I_r_d	0.95	0.95	0.01	0.11	0.11	0.00	0.00
V_r_q	0.09	0.09	0.01	0.94	0.94	0.00	0.00
V_r_d	0.16	0.16	0.01	1.00	1.00	0.00	0.00
I_dci_1	0.00	0.00	0.00	0.00	0.00	0.00	0.00
etheta_i	0.00	0.00	0.00	0.00	0.00	0.41	0.00
U_i_d	0.00	0.00	0.00	0.00	0.00	0.00	0.00
P_dcr	0.00	0.00	1.00	0.02	0.02	0.00	0.02
etheta_r	0.00	0.00	0.10	0.02	0.02	0.00	1.00
U_r_d	0.00	0.00	0.00	0.00	0.00	0.00	0.02

Mode	8	9	10	11	12	13
Damping	0.01	0.01	0.10	0.10	1.00	1.00
Frequency(Hz)	75.61	75.61	17.55	17.55	5.13	2.83
I_dcr	0.31	0.31	1.00	1.00	0.11	0.03
I_dci	0.89	0.89	0.34	0.34	0.05	0.01
V_dc	1.00	1.00	0.17	0.17	0.00	0.01
V_dci	0.18	0.18	0.93	0.93	0.00	0.02
I_i_d	0.00	0.00	0.00	0.00	0.00	0.00
I_i_q	0.00	0.00	0.00	0.00	0.00	0.00
int V_dcr	0.00	0.00	0.03	0.03	0.15	1.00
int I_i_d (ms)	0.00	0.00	0.00	0.00	0.00	0.00
int I_i_q (ms)	0.00	0.00	0.00	0.00	0.00	0.00
I_r_q	0.00	0.00	0.00	0.00	0.00	0.00
I_r_d	0.01	0.01	0.03	0.03	0.01	0.00
V_r_q	0.00	0.00	0.00	0.00	0.00	0.00
V_r_d	0.00	0.00	0.00	0.00	0.00	0.00
I_dci_1	0.00	0.00	0.19	0.19	1.00	0.20
etheta_i	0.00	0.00	0.00	0.00	0.00	0.00
U_i_d	0.00	0.00	0.00	0.00	0.00	0.00
P_dcr	0.01	0.01	0.02	0.02	0.00	0.00
etheta_r	0.01	0.01	0.04	0.04	0.01	0.01
U_r_d	0.00	0.00	0.00	0.00	0.01	0.01

Mode	14	15	16	17	18	19
Damping	1.00	1.00	0.75	0.75	1.00	1.00
Frequency(Hz)	1.61	3.41	149.54	149.54	1.47	1.27
I_dcr	0.00	0.00	0.00	0.00	0.00	0.00
I_dci	0.00	0.00	0.00	0.00	0.00	0.00
V_dc	0.00	0.00	0.00	0.00	0.00	0.00
V_dci	0.00	0.00	0.00	0.00	0.00	0.00
I_i_d	0.00	0.00	0.49	0.49	0.00	0.00
I_i_q	0.00	0.00	0.93	0.93	0.00	0.00
int V_dcr	0.01	0.00	0.00	0.00	0.00	0.00
int I_i_d (ms)	0.00	1.00	0.01	0.01	0.02	0.03
int I_i_q (ms)	0.00	0.03	0.04	0.04	0.48	1.00
I_r_q	0.00	0.00	0.00	0.00	0.00	0.00
I_r_d	0.00	0.00	0.00	0.00	0.00	0.00
V_r_q	0.00	0.00	0.00	0.00	0.00	0.00
V_r_d	0.00	0.00	0.00	0.00	0.00	0.00
I_dci_1	0.00	0.00	0.00	0.00	0.00	0.00
etheta_i	0.00	0.00	1.00	1.00	0.08	0.07
U_i_d	0.00	0.00	0.01	0.01	1.00	0.33
P_dcr	0.00	0.00	0.00	0.00	0.00	0.00
etheta_r	0.01	0.00	0.00	0.00	0.00	0.00
U_r_d	1.00	0.00	0.00	0.00	0.00	0.00

Table C.3 Natural frequency and damping of hybrid configuration 2 small signal model poles

Frequency(Hz)	Damping
1023.44	1.00
346.94	0.06
346.94	0.06
161.38	1.00
220.79	0.02
220.79	0.02
207.96	0.00
207.96	0.00
96.43	1.00
222.84	0.54
222.84	0.54
91.02	1.00
57.88	0.05
57.88	0.05
59.57	1.00
3.56	1.00
3.97	1.00
3.97	1.00
0.80	1.00
1.62	1.00
1.62	1.00

Table C.4 Partifipation factors of hybrid configuration 2

Mode	1	2	3	4	5	6	7
Damping	1.00	0.06	0.06	1.00	0.02	0.02	(0.00)
Frequency(Hz)	1023.44	346.94	346.94	161.38	220.79	220.79	207.96
I_dcr	1.00	0.00	0.00	0.02	0.00	0.00	0.00
I_dci	0.00	0.01	0.01	0.00	0.00	0.00	0.00
V_dc	0.00	0.00	0.00	0.00	0.00	0.00	0.00
V_dci	0.00	0.70	0.70	0.00	0.00	0.00	0.00
I_i_d	0.00	0.05	0.05	0.00	0.00	0.00	0.00
I_i_q	0.00	1.00	1.00	0.00	0.00	0.00	0.00
int Idcr*	0.00	0.00	0.00	0.00	0.00	0.00	0.00
I_r_q	0.00	0.00	0.00	0.00	1.00	1.00	0.19
I_r_d	0.00	0.00	0.00	0.01	0.97	0.97	0.22
V_r_q	0.00	0.00	0.00	0.00	0.20	0.20	0.97
V_r_d	0.00	0.00	0.00	0.01	0.18	0.18	1.00
int I_i_d (ms)	0.00	0.00	0.00	0.00	0.00	0.00	0.00
int I_i_q (ms)	0.00	0.01	0.01	0.00	0.00	0.00	0.00
I_i_d (ms)	0.00	0.12	0.12	0.00	0.00	0.00	0.00
I_i_q (ms)	0.00	0.28	0.28	0.00	0.00	0.00	0.00
int V_dci	0.00	0.00	0.00	0.00	0.00	0.00	0.00
etheta_i	0.00	0.10	0.10	0.00	0.00	0.00	0.00
U_i_d	0.00	0.00	0.00	0.00	0.00	0.00	0.00
P_dcr	0.00	0.00	0.00	1.00	0.00	0.00	0.00
etheta_r	0.00	0.00	0.00	0.04	0.00	0.00	0.00
U_r_d	0.00	0.00	0.00	0.00	0.00	0.00	0.00

Mode	8	9	10	11	12	13	14
Damping	(0.00)	1.00	0.54	0.54	1.00	0.05	0.05
Frequency(Hz)	207.96	96.43	222.84	222.84	91.02	57.88	57.88
I_dcr	0.00	0.02	0.00	0.00	0.00	0.00	0.00
I_dci	0.00	0.00	0.00	0.00	0.02	1.00	1.00
V_dc	0.00	0.00	0.00	0.00	0.01	0.95	0.95
V_dci	0.00	0.00	0.17	0.17	0.23	0.02	0.02
I_i_d	0.00	0.00	0.99	0.99	0.19	0.00	0.00
I_i_q	0.00	0.00	0.06	0.06	0.06	0.01	0.01
int Idcr*	0.00	0.00	0.00	0.00	0.00	0.00	0.00
I_r_q	0.19	0.00	0.00	0.00	0.00	0.00	0.00
I_r_d	0.22	0.00	0.00	0.00	0.00	0.00	0.00
V_r_q	0.97	0.00	0.00	0.00	0.00	0.00	0.00
V_r_d	1.00	0.00	0.00	0.00	0.00	0.00	0.00
int I_i_d (ms)	0.00	0.00	0.02	0.02	0.01	0.00	0.00
int I_i_q (ms)	0.00	0.00	0.00	0.00	0.02	0.00	0.00
I_i_d (ms)	0.00	0.00	1.00	1.00	0.03	0.00	0.00
I_i_q (ms)	0.00	0.00	0.07	0.07	1.00	0.02	0.02
int V_dci	0.00	0.00	0.00	0.00	0.00	0.00	0.00
etheta_i	0.00	0.00	0.38	0.38	0.37	0.03	0.03
U_i_d	0.00	0.00	0.00	0.00	0.01	0.00	0.00
P_dcr	0.00	0.01	0.00	0.00	0.00	0.00	0.00
etheta_r	0.00	1.00	0.00	0.00	0.00	0.00	0.00
U_r_d	0.00	0.02	0.00	0.00	0.00	0.00	0.00

Mode	15	16	17	18	19	20	21
Damping	1.00	1.00	1.00	1.00	1.00	1.00	1.00
Frequency(Hz))	59.57	3.56	3.97	3.97	0.80	1.62	1.62
I_dcr	0.00	0.00	0.00	0.00	0.00	0.00	0.00
I_dci	0.02	0.00	0.00	0.00	0.00	0.00	0.00
V_dc	0.02	0.00	0.01	0.01	0.00	0.00	0.00
V_dci	0.20	0.00	0.02	0.02	0.00	0.00	0.00
I_i_d	0.05	0.01	0.01	0.01	0.00	0.00	0.00
I_i_q	0.01	0.00	0.00	0.00	0.00	0.00	0.00
int Idcr*	0.00	0.00	1.00	1.00	0.00	0.00	0.00
I_r_q	0.00	0.00	0.00	0.00	0.00	0.00	0.00
I_r_d	0.00	0.00	0.00	0.00	0.00	0.00	0.00
V_r_q	0.00	0.00	0.00	0.00	0.00	0.00	0.00
V_r_d	0.00	0.00	0.00	0.00	0.00	0.00	0.00
int I_i_d (ms)	0.00	1.00	0.08	0.08	0.00	0.00	0.00
int I_i_q (ms)	0.04	0.07	0.93	0.93	0.02	0.00	0.00
I_i_d (ms)	0.09	0.00	0.00	0.00	0.00	0.00	0.00
I_i_q (ms)	0.18	0.00	0.00	0.00	0.00	0.00	0.00
int V_dci	0.00	0.00	0.03	0.03	1.00	0.00	0.00
etheta_i	1.00	0.00	0.01	0.01	0.00	0.00	0.02
U_i_d	0.03	0.00	0.01	0.01	0.00	0.01	1.00
P_dcr	0.00	0.00	0.00	0.00	0.00	0.00	0.00
etheta_r	0.00	0.00	0.00	0.00	0.00	0.02	0.00
U_r_d	0.00	0.00	0.00	0.00	0.00	1.00	0.01

Table C.5 Natural frequency and damping of hybrid configuration 3 small signal model poles

Frequency(Hz)	Damping
2611.71	1.00
282.54	1.00
96.22	1.00
253.87	0.49
253.87	0.49
222.50	0.02
222.50	0.02
209.87	0.00
209.87	0.00
60.43	0.06
60.43	0.06
9.92	1.00
3.82	1.00
3.49	1.00
0.04	1.00
1.62	1.00
1.71	1.00
0.78	1.00

Table C.6 Natural frequency and damping of hybrid configuration 3 small signal model poles

Mode	1	2	3	4	5	6	7	8	9
Damping	1.00	1.00	1.00	0.49	0.49	0.02	0.02	0.00	0.00
Frequency(Hz)	2611.71	282.54	96.22	253.87	253.87	222.50	222.50	209.87	209.87
I_dcr	0.00	0.00	0.00	0.01	0.01	0.00	0.00	0.00	0.00
I_dci	1.00	0.00	0.01	0.00	0.00	0.00	0.00	0.02	0.02
V_dc	0.00	0.00	0.00	0.00	0.00	0.00	0.00	0.00	0.00
V_dci	0.00	0.09	0.00	0.67	0.67	0.00	0.00	0.00	0.00
int I_dcr	0.00	0.00	0.00	0.00	0.00	0.00	0.00	0.00	0.00
I_i_q	0.00	0.00	0.00	0.00	0.00	1.00	1.00	0.19	0.19
I_i_d	0.00	0.00	0.00	0.00	0.00	0.98	0.98	0.34	0.34
V_i_q	0.00	0.00	0.00	0.00	0.00	0.33	0.33	0.98	0.98
V_i_d	0.00	0.00	0.00	0.00	0.00	0.18	0.18	1.00	1.00
int I_r_d (ms)	0.00	0.01	0.00	0.00	0.00	0.00	0.00	0.00	0.00
int I_r_q (ms)	0.00	0.00	0.00	0.01	0.01	0.00	0.00	0.00	0.00
int V_dcr	0.00	0.00	0.00	0.00	0.00	0.00	0.00	0.00	0.00
I_r_d	0.00	1.00	0.00	0.02	0.02	0.00	0.00	0.00	0.00
I_r_q	0.00	0.07	0.00	1.00	1.00	0.00	0.00	0.00	0.00
etheta_r	0.00	0.13	0.00	0.33	0.33	0.00	0.00	0.00	0.00
U_r_d	0.00	0.00	0.00	0.00	0.00	0.00	0.00	0.00	0.00
etheta_i	0.00	0.00	1.00	0.00	0.00	0.00	0.00	0.01	0.01
U_i_d	0.00	0.00	0.02	0.00	0.00	0.00	0.00	0.00	0.00

Mode	10	11	12	13	14	15	16	17	18
Damping	0.06	0.06	1.00	1.00	1.00	1.00	1.00	1.00	1.00
Frequency(Hz)	60.43	60.43	9.92	3.82	3.49	0.04	1.62	1.71	0.78
I_dcr	1.00	1.00	0.01	0.00	0.00	0.00	0.00	0.00	0.00
I_dci	0.00	0.00	0.00	0.00	0.00	0.00	0.00	0.00	0.00
V_dc	0.87	0.87	0.36	0.03	0.01	0.00	0.00	0.00	0.00
V_dci	0.08	0.08	1.00	0.08	0.03	0.00	0.00	0.00	0.00
int I_dcr	0.00	0.00	0.00	0.00	0.00	1.00	0.00	0.00	0.00
I_i_q	0.00	0.00	0.00	0.00	0.00	0.00	0.00	0.00	0.00
I_i_d	0.00	0.00	0.00	0.00	0.00	0.00	0.00	0.00	0.00
V_i_q	0.00	0.00	0.00	0.00	0.00	0.00	0.00	0.00	0.00
V_i_d	0.00	0.00	0.00	0.00	0.00	0.00	0.00	0.00	0.00
int I_r_d (ms)	0.00	0.00	0.31	1.00	0.44	0.00	0.00	0.01	0.00
int I_r_q (ms)	0.00	0.00	0.33	0.33	1.00	0.00	0.00	0.03	0.04
int V_dcr	0.00	0.00	0.06	0.01	0.00	0.00	0.00	0.01	1.00
I_r_d	0.02	0.02	0.43	0.05	0.00	0.00	0.00	0.00	0.00
I_r_q	0.02	0.02	0.05	0.00	0.00	0.00	0.00	0.00	0.00
etheta_r	0.06	0.06	0.97	0.02	0.00	0.00	0.00	0.08	0.00
U_r_d	0.00	0.00	0.18	0.01	0.00	0.00	0.00	1.00	0.00
etheta_i	0.00	0.00	0.00	0.00	0.00	0.00	0.02	0.00	0.00
U_i_d	0.00	0.00	0.00	0.00	0.00	0.00	1.00	0.00	0.00

Table C.7 Natural frequency and damping of hybrid configuration 4 small signal model poles

Frequency(Hz)	Damping
222.19	0.02
222.19	0.02
209.58	0.00
209.58	0.00
97.45	1.00
75.20	0.01
75.20	0.01
244.06	1.00
18.68	0.14
18.68	0.14
0.13	1.00
179.85	0.96
179.85	0.96
1.62	1.00
3.55	1.00
1.48	1.00
1.25	1.00

Table C.8 Partifipation factors of hybrid configuration 4

Mode	1	2	3	4	5	6	7	8	9
Damping	0.02	0.02	0.00	0.00	1.00	0.01	0.01	1.00	0.14
Frequency(Hz)	222.19	222.19	209.58	209.58	97.45	75.20	75.20	244.06	18.68
I_dcr	0.00	0.00	0.00	0.00	0.00	0.90	0.90	0.00	0.29
I_dci	0.00	0.00	0.00	0.00	0.00	0.29	0.29	0.00	0.90
V_dc	0.00	0.00	0.00	0.00	0.00	1.00	1.00	0.00	0.19
V_dcr	0.00	0.00	0.00	0.00	0.00	0.19	0.19	0.00	1.00
I_i_q	1.00	1.00	0.20	0.20	0.00	0.00	0.00	0.00	0.00
I_i_d	0.99	0.99	0.20	0.20	0.00	0.00	0.00	0.00	0.00
V_i_q	0.19	0.19	0.99	0.99	0.00	0.00	0.00	0.00	0.00
V_i_d	0.19	0.19	1.00	1.00	0.00	0.00	0.00	0.00	0.00
int I_r_d (ms)	0.00	0.00	0.00	0.00	0.00	0.00	0.00	0.02	0.00
int I_r_q (ms)	0.00	0.00	0.00	0.00	0.00	0.00	0.00	0.01	0.00
I_r_d	0.00	0.00	0.00	0.00	0.00	0.00	0.00	1.00	0.00
I_r_q	0.00	0.00	0.00	0.00	0.00	0.00	0.00	0.58	0.00
etheta_r	0.00	0.00	0.00	0.00	0.00	0.00	0.00	0.00	0.00
U_r_d	0.00	0.00	0.00	0.00	0.00	0.00	0.00	0.00	0.00
etheta_i	0.00	0.00	0.00	0.00	1.00	0.00	0.00	0.00	0.00
U_i_d	0.00	0.00	0.00	0.00	0.02	0.00	0.00	0.00	0.00
int Vdci	0.00	0.00	0.00	0.00	0.00	0.00	0.00	0.00	0.00

Mode	10	11	12	13	14	15	16	17
Damping	0.14	1.00	0.96	0.96	1.00	1.00	1.00	1.00
Frequency(Hz)	18.68	0.13	179.85	179.85	1.62	3.55	1.48	1.25
I_dcr	0.29	0.00	0.00	0.00	0.00	0.00	0.00	0.00
I_dci	0.90	0.00	0.00	0.00	0.00	0.00	0.00	0.00
V_dc	0.19	0.00	0.00	0.00	0.00	0.00	0.00	0.00
V_dcr	1.00	0.00	0.00	0.00	0.00	0.00	0.00	0.00
I_i_q	0.00	0.00	0.00	0.00	0.00	0.00	0.00	0.00
I_i_d	0.00	0.00	0.00	0.00	0.00	0.00	0.00	0.00
V_i_q	0.00	0.00	0.00	0.00	0.00	0.00	0.00	0.00
V_i_d	0.00	0.00	0.00	0.00	0.00	0.00	0.00	0.00
int I_r_d (ms)	0.00	0.00	0.01	0.01	0.00	1.00	0.00	0.01
int I_r_q (ms)	0.00	0.00	0.03	0.03	0.00	0.02	0.38	1.00
I_r_d	0.00	0.00	0.57	0.57	0.00	0.01	0.00	0.00
I_r_q	0.00	0.00	1.00	1.00	0.00	0.00	0.00	0.00
etheta_r	0.00	0.00	0.41	0.41	0.00	0.00	0.07	0.06
U_r_d	0.00	0.00	0.00	0.00	0.00	0.00	1.00	0.28
etheta_i	0.00	0.00	0.00	0.00	0.02	0.00	0.00	0.00
U_i_d	0.00	0.00	0.00	0.00	1.00	0.00	0.00	0.00
int Vdci	0.00	1.00	0.00	0.00	0.00	0.00	0.00	0.00

Appendix D. Budget of The Thesis

Working Hours

The cost for working hours contains the labor cost the author spent on the thesis and relative work. Also, the working hours of the thesis work supervision should also be considered.

Table D.1 Working hours costs of the thesis

Concept	Working hours	Hourly wage (€)	Total (€)
Author's Research Work	600	12	7,200
Supervision Work	200	20	4,000
Total (€)			11,200

Equipment and Tools

The cost of items involved in the development of this thesis includes the necessary tool and access to required digital information and service.

Table D.2 Tool costs of the Thesis

Concept	Cost(€)
Personal Computer (Mi Air 13.3' portable computer)	800
MATLAB Suite annual license for student	69
MathType software annual license for student	30
One-year access to IEEE digital library	50
Total (€)	949

Bibliography

[1] O. E. Oni, K. I. Mbangula, and I. E. Davidson, "A Review of LCC-HVDC and VSC-HVDC Technologies and Applications," vol. 1, no. 3, 2016.

[2] D. Jovcic *et al.*, "High Voltage Direct Current Transmission : Converters, Systems, and DC Grids," *CEUR Workshop Proc.*, 2011.

[3] M. H. Nguyen, T. K. Saha, and M. Eghbal, "Hybrid multi-terminal LCC HVDC with a VSC Converter: A case study of Simplified South East Australian system," *IEEE Power Energy Soc. Gen. Meet.*, pp. 1–8, 2012.

[4] Z. Zhao and M. R. Iravani, "Application of GTO voltage source inverter in a hybrid HVDC link," *IEEE Trans. Power Deliv.*, vol. 9, no. 1, pp. 369–377, 1994.

[5] X. Chen *et al.*, "Integrating wind farm to the grid using hybrid multiterminal HVDC technology," *IEEE Trans. Ind. Appl.*, vol. 47, no. 2, pp. 965–972, 2011.

[6] Y. Lee, S. Cui, S. Kim, and S. K. Sul, "Control of hybrid HVDC transmission system with LCC and FB-MMC," *2014 IEEE Energy Convers. Congr. Expo. ECCE 2014*, pp. 475–482, 2014.

[7] Y. Huang, W. Huang, M. Li, and T. Liu, "Steady-state control strategy of multi-terminal hybrid UHVDC," *2017 19th Eur. Conf. Power Electron. Appl. EPE 2017 ECCE Eur.*, vol. 2017–Janua, pp. 1–10, 2017.

[8] P. Manohar, V. Kelamane, D. Kaushik, and W. Ahmed, "Improved controls for LCC-VSC hybrid HVDC system," *2013 Int. Conf. Circuits, Control. Commun. CCUBE 2013*, 2013.

[9] L. Chetty, "Lcc Hvdc Control Systems," no. September, pp. 1–128, 2011.

[10] N. Mohan, T. M. Undeland, and W. P. Robbins, *Power Electronics Converters, Applications, and Design*. 2007.

[11] H. U. A. N. G. Ying, S. Key, E. Power, and P. Grid, "Design of AC Filter for HVDC Transmission Project Adopting Common Station and Double-circuit on the Same Tower."

[12] A. Yazdani and R. Iravani, *Voltage-Sourced Converters in Power Systems: Modeling, Control, and Applications*. 2010.

[13] P. Li and Q. Hao, "The algorithm for the parameters of AC filters in HVDC transmission system," *Transm. Distrib. Expo. Conf. 2008 IEEE PES Powering Towar. Futur. PIMS 2008*, pp. 1–6, 2008.

[14] M. H. Nguyen, T. K. Saha, and M. Eghbal, "Master self-tuning VDCOL function for hybrid multi-terminal HVDC connecting renewable resources to a large power

system," *IET Gener. Transm. Distrib.*, 2017.

[15] Guo Chunyi, Zhao Chengyong, and Liu Wenjing, "The control strategy for Hybrid HVDC using voltage margin control and voltage dependent current order limiter control," *2nd IET Renew. Power Gener. Conf. (RPG 2013)*, p. 2.57-2.57, 2013.

[16] S. Liberty, "Modern control engineering," *IEEE Trans. Automat. Contr.*, 1972.

[17] M. Daryabak *et al.*, "Modeling of LCC-HVDC systems using dynamic phasors," *IEEE Trans. Power Deliv.*, vol. 29, no. 4, pp. 1989–1998, 2014.

[18] M. O. Faruque, Y. Zhang, and V. Dinavahi, "Detailed modeling of CIGRÉ HVDC benchmark system using PSCAD/EMTDC and PSB/SIMULINK," *IEEE Trans. Power Deliv.*, vol. 21, no. 1, pp. 378–387, 2006.

[19] R. Rogersten, "VSC HVDC System Modelling and Validation," *KTH*, 2014.

[20] A. Egea-Alvarez, A. Junyent-Ferre, and O. Gomis Bellmunt, "Active and reactive power control of grid connected distributed generation systems," pp. 1–35, 2000.

[21] L. Harnefors and H.-P. Nee, "Model-based current control of AC machines using the internal model\ncontrol method," *IEEE Trans. Ind. Appl.*, 1998.

[22] CIGRE WG B4.46, *Voltage Source Converter (VSC) HVDC for Power Transmission - Economic Aspects and Comparison with other AC and DC Technologies*. 2012.

[23] R. E. Torres-Olguin and A. Garces, "Grid Integration of offshore wind farms using a Hybrid HVDC composed by an MMC with an LCC-based transmission system," *Energy Procedia*, vol. 137, pp. 391–400, 2017.

[24] G. Kalcon, G. Adam, O. Anaya-Lara, S. Lo, and K. Uhlen, "Small - Signal Stability Analysis of Multi - Terminal VSC - Based DC Transmission Systems," *IEEE Trans. Power Syst.*, 2012.

[25] C. Karawita and U. Annakkage, "Multi-In-Feed HVDC interaction studies using small signal stability assessment," *2009 IEEE Power Energy Soc. Gen. Meet.*, 2009.

[26] X. Yang and C. Chen, "HVDC Dynamic modelling for small signal analysis," *IEE Proc. - Gener. Transm. Distrib.*, 2004.

[27] P. S. Kundur, "Power System Stability and Control," *Library of Congress Cataloging-in-Publication Data*. p. 1179, 1994.

[28] G. Instantaneous and R. Power, "Generalized instantaneous reactive power theory for three-phase power systems," *IEEE Trans. Instrum. Meas.*, 1996.

[29] E. Prieto-Araujo, A. Egea-Alvarez, S. Fekriasl, and O. Gomis-Bellmunt, "DC voltage droop control design for multi-terminal HVDC systems considering AC and DC grid dynamics," *IEEE Trans. Power Deliv.*, vol. PP, no. 99, pp. 1–11, 2015.

[30] O. Kotb, M. Ghandhari, R. Eriksson, and V. K. Sood, "A study on the control of a hybrid MTDC system supplying a passive network," *POWERCON 2014 - 2014 Int. Conf. Power Syst. Technol. Towar. Green, Effic. Smart Power Syst. Proc.*, no. Powercon, pp. 2427–2432, 2014.

[31] A. H. Nordstrom, "Challenges and opportunities aplety: How to meet the challenge of climate change," *ABB Rev.*, 2009.

[32] Alstom Grid, "HVDC-VSC : transmission technology of the future," *Think Grid*, 2011.